

# Spin non-Collinear Real-Time Time-Dependent Density-Functional Theory and Implementation in the Modern GPU-Accelerated INQ code

Jacopo Simoni,<sup>\*,†</sup> Xavier Andrade,<sup>‡</sup> Wuzhang Fang,<sup>†</sup> Andrew C. Grieder,<sup>†</sup>  
Alfredo A. Correa,<sup>‡</sup> Tadashi Ogitsu,<sup>‡</sup> and Yuan Ping<sup>†,¶,§</sup>

<sup>†</sup>*Department of Materials Science and Engineering, University of Wisconsin, Madison, WI, 53706, USA*

<sup>‡</sup>*Lawrence Livermore National Laboratory*

<sup>¶</sup>*Department of Physics, University of Wisconsin, Madison, WI, 53706, USA*

<sup>§</sup>*Department of Chemistry, University of Wisconsin, Madison, WI, 53706, USA*

E-mail: jsimoni@wisc.edu

## Abstract

Time-dependent density functional theory (TDDFT) is a theory that describes the time evolution of quantum mechanical many-electron systems under the influence of external time-dependent electric and magnetic fields. INQ is a specially designed software to efficiently solve the real-time TDDFT equations on graphics processing units (GPUs), which aim to overcome the computational limitation of time and size scales of non-equilibrium quantum dynamics. In this work we will present an implementation of non-collinear TDDFT for the INQ code to simulate spin dynamics in real time and discuss the implementation of non-collinear magnetic effects into the code. We will discuss the implementation of exchange-correlation magnetic fields, spin-orbit coupling, and the interaction between the electronic system and external magnetic fields. We will then consider several prototypical examples of spin dynamics in magnetic clusters and solids after light excitation. Potential applications range from the study of real-time dynamics of magnons to ultrafast spin dynamics under linear and circularly polarized laser excitation, as well as spectroscopic signatures such as mag-

netic circular dichroism and pump-probe Kerr rotation.

## 1 Introduction

Magnetism is a fundamental interaction in nature that is responsible for the attractive and repulsive forces observed in magnetic materials. Localized magnetic moments can interact and cause macroscopic-magnetic ordering. Ferromagnetism and anti-ferromagnetism are the simplest forms of such macroscopic ordering; their origin is quantum mechanical and determined by the exchange interaction and the Pauli exclusion principle. Magnetic anisotropy is instead a measure of the coupling between spin and spatial degrees of freedom in a material. This is determined at the atomic level by the spin-orbit interaction. A correct ab-initio description of the magnetic properties of materials must be able to capture these different interactions.<sup>1</sup>

The success of density functional theory (DFT) in describing the magnetic properties of materials can be ascribed to its ability to account for exchange interactions, via the exchange-correlation potential, and magnetic anisotropy through the spin-orbit interaction.<sup>2</sup>

Although DFT is a formally exact approach to the calculation of the ground state of electronic systems, in practice, the exact exchange-correlation functional is unknown and approximations must be considered. Local-density approximations have been shown to be quite successful in describing the equilibrium magnetic properties<sup>3</sup> and the slow adiabatic dynamics in solids.<sup>4,5</sup>

The aim of time-dependent density functional theory (TDDFT) is to extend this success to linear response properties and to the real-time domain.<sup>6</sup> Under non-equilibrium conditions, the exchange interactions become dynamical, and the simple picture of Heisenberg exchange breaks down. To overcome this problem, electronic degrees of freedom should also evolve dynamically.

Out-of-equilibrium dynamics in magnetic systems is important for many different applications including spintronics<sup>7</sup> and orbitronics,<sup>8,9</sup> quantum computation,<sup>10</sup> skyrmion dynamics for magnetic storage technologies,<sup>11–13</sup> ultrafast magnetism,<sup>14</sup> spin and orbital momentum dynamics in chiral systems,<sup>15</sup> the chiral-induced spin selectivity (CISS) effect<sup>16</sup> and collinear spin and orbital Edelstein effect in solids.<sup>17</sup>

Ultrafast magnetism describes the sub-picosecond dynamics of magnetic systems under the application of intense laser pulses. The complete demagnetization of a Ni film has been experimentally demonstrated.<sup>18</sup> Later, other experiments confirmed such findings and have shown the possibility of laser-induced spin re-orientation and modification of the magnetic structure.<sup>19–21</sup> Femtomagnetism is a research field that focuses on the control of the magnetic order in materials using femtosecond laser pulses and has two main goals: (i) a better understanding of the physics of light-induced spin dynamics on very short time scales; (ii) control and manipulation of the spin degrees of freedom on sub-picosecond time scales. The uncertainty on the underlying physical mechanism responsible for this phenomenon makes TDDFT a particularly attractive approach to studying such phenomena.

In the CISS effect, the transmission probability of electrons through a chiral molecule

depends on the electron’s spin state, generating spin polarized electrons.<sup>22</sup> This has important implications in catalysis,<sup>23</sup> enantio-separation<sup>24</sup> and spintronics.<sup>25</sup> No complete theoretical description is available at the moment; however, there is a general consensus on the fact that a correct description of the interplay between spin-orbit, electron-electron and electron-phonon interactions is required to reproduce such an effect.<sup>26–28</sup> The non-collinear formulation of TDDFT, thanks to its ability to treat spin-orbit non-perturbatively and include electronic correlations, is potentially applicable to studying such an effect.

Spin-wave excitations are considered promising information carriers in spintronics due to their low energy consumption and fast speed of operation.<sup>29</sup> Non-perturbative schemes to compute the magnetic excitation spectrum in extended systems within TDDFT have been proposed.<sup>30</sup> This has potential applications in the field of magnonics<sup>31</sup> and quantum magnonics,<sup>32,33</sup> which is based on the idea of magnons as quantum information carriers.

Several implementations of real-time TDDFT are already available based on real-space multi-grids<sup>34</sup> (within the RMG code), NWChem has an implementation based on Gaussian basis sets.<sup>35</sup> **Octopus**<sup>36,37</sup> works on a real-space grid and can be used to perform real-time simulation of spin-polarized systems, **Elk**<sup>38</sup> is a full-potential linearized augmented plane-waves (FP-LAPW) code working for crystalline solids that can also simulate real-time evolution of magnetic systems. The **INQ** code<sup>39</sup> is designed to provide a coherent and computationally efficient framework for the implementation of TDDFT that can make use of large GPU-based supercomputers. **INQ** is a streamlined implementation of DFT and TDDFT that is very compact, only 12,000 lines of code, and that is easy to maintain and further develop. Here we discuss the implementation of non-collinear spin DFT and TDDFT in the code, which provides an accurate and efficient tool to study various spin-related phenomena in and out of equilibrium.

In section (2) we discuss the theoretical background required for the non-collinear spin DFT implementation. In section (3) we present the

details of the implementation. In section (4) we present results and a comparison with other codes by looking in particular at the dynamics under external electric and magnetic pulses.

## 2 Theoretical background

Before introducing the non-collinear version of spin DFT in subsection (2.2) we briefly discuss the collinear version in (2.1). TDDFT and its non-collinear version are discussed in sections (2.3) and (2.4). In the remaining part of the theory section, we analyze the approximations used to implement the non-collinear equations in INQ.

### 2.1 Density Functional Theory for spin polarized systems

DFT has been a widely successful theory for the calculation of electronic structures in both molecules and materials.<sup>40</sup> The basic formalism of DFT is given by the Kohn-Sham (KS) equation<sup>41</sup> (atomic units are used throughout)

$$\left[ -\frac{1}{2}\nabla^2 + v_{\text{KS}}[n](\mathbf{r}) \right] \psi_i^{\text{KS}}(\mathbf{r}) = \varepsilon_i^{\text{KS}} \psi_i^{\text{KS}}(\mathbf{r}), \quad (1)$$

where  $\varepsilon_i^{\text{KS}}$  and  $\psi_i^{\text{KS}}(\mathbf{r})$  correspond to the KS energy eigenvalues and eigenstates.  $v_{\text{KS}}(\mathbf{r})$  is the KS potential, a functional of the electron density given by the sum of three terms: the external potential due to the surrounding ions, the Hartree, and the exchange-correlation potentials and can be written as

$$\begin{aligned} v_{\text{KS}}[n](\mathbf{r}) &= v_{\text{ext}}(\mathbf{r}) + v_{\text{H}}[n](\mathbf{r}) + v_{\text{xc}}[n](\mathbf{r}) \\ &= -\sum_a \frac{Z_a}{|\mathbf{r} - \mathbf{R}_a|} + \int d\mathbf{r}' \frac{n(\mathbf{r}')}{|\mathbf{r} - \mathbf{r}'|} + v_{\text{xc}}[n](\mathbf{r}). \end{aligned} \quad (2)$$

Eq. (1) and (2) cannot be directly applied to magnetic systems. Spin density functional theory (SDFT)<sup>42</sup> requires the extension of Eq. (1) for spin-polarized systems through the introduction of two dynamical variables:  $n_\alpha(\mathbf{r})$  with  $\alpha = 0, 1$ . These correspond to the spin-up and spin-down densities respectively. This is the so-

called spin-unrestricted formulation of DFT.<sup>43</sup> The direction of spin polarization is arbitrary, but it is usually taken along the  $z$  axis. In the presence of an external magnetic field  $b_{\text{ext}}(\mathbf{r})$ , SDFT yields the equation,

$$\left[ -\frac{1}{2}\nabla^2 + v_{\text{KS}}^\alpha[n_0, n_1](\mathbf{r}) + (-1)^\alpha \mu_{\text{B}} b_{\text{ext}}(\mathbf{r}) \right] \psi_{i\alpha}^{\text{KS}}(\mathbf{r}) = \varepsilon_{i\alpha}^{\text{KS}} \psi_{i\alpha}^{\text{KS}}(\mathbf{r}). \quad (3)$$

Here, the two density components are obtained from  $n_\alpha(\mathbf{r}) = \sum_i f_{i\alpha} |\psi_{i\alpha}^{\text{KS}}(\mathbf{r})|^2$ , with  $f_{i\alpha}$  indicating the state occupation.  $\varepsilon_{i\alpha}^{\text{KS}}$  are the KS eigenvalues for the spin-up and down states.  $\mu_{\text{B}}$  is the Bohr magneton (1/2 in atomic units).

Eq. (3) is usually expressed in terms of the total charge density  $n(\mathbf{r}) = n_0(\mathbf{r}) + n_1(\mathbf{r})$ , and the spin density along the quantization axis of the system,  $m(\mathbf{r}) = n_0(\mathbf{r}) - n_1(\mathbf{r})$ . This results in

$$\begin{aligned} \bar{v}_{\text{KS}}[n, m](\mathbf{r}) &= \frac{\sum_\alpha v_{\text{KS}}^\alpha(\mathbf{r})}{2} = \\ &= v_{\text{ext}}(\mathbf{r}) + v_{\text{H}}[n](\mathbf{r}) + \bar{v}_{\text{xc}}[n, m](\mathbf{r}) \end{aligned} \quad (4)$$

$$\bar{v}_{\text{xc}}[n, m](\mathbf{r}) = \frac{v_{\text{xc}}^0(\mathbf{r}) + v_{\text{xc}}^1(\mathbf{r})}{2} \quad (5)$$

$$\begin{aligned} b_{\text{xc}}[n, m](\mathbf{r}) &= \frac{\sum_\alpha (-1)^\alpha v_{\text{KS}}^\alpha(\mathbf{r})}{2} = \\ &= \frac{v_{\text{xc}}^0[n, m](\mathbf{r}) - v_{\text{xc}}^1[n, m](\mathbf{r})}{2} \end{aligned} \quad (6)$$

$$b_{\text{s}}[n, m](\mathbf{r}) = \mu_{\text{B}} b_{\text{ext}}(\mathbf{r}) + b_{\text{xc}}[n, m](\mathbf{r}). \quad (7)$$

By using this new set of variables, the KS Hamiltonian can then be expressed in the spin space as a  $2 \times 2$  matrix.

$$\begin{aligned} \mathcal{H}_{\text{KS}}(\mathbf{r}) &= \left[ -\frac{1}{2}\nabla^2 + v_{\text{ext}}(\mathbf{r}) + v_{\text{H}}[n](\mathbf{r}) + \right. \\ &\quad \left. + \bar{v}_{\text{xc}}[n, m](\mathbf{r}) \right] \mathbf{I}_2 + b_{\text{s}}[n, m](\mathbf{r}) \sigma_z, \end{aligned} \quad (8)$$

$\sigma_z$  is the  $z$  component of the Pauli matrices and  $\mathbf{I}_2$  is the  $2 \times 2$  identity matrix. Eq. (8) has a strong limitation: It does not allow the spin to rotate. This means that we need to generalize the equations of collinear SDFT if we want to perform spin dynamics. We discuss how this can be done in the next section.

## 2.2 Non-collinear formulation of spin DFT

In the Hamiltonian of Eq. (8) the spin is always projected along the z axis. This means that the spin cannot rotate and that the Hamiltonian of the system commutes with  $\sigma_z$ ,  $[\mathcal{H}_{\text{KS}}(\mathbf{r}), \sigma_z] = 0$ .

The KS eigenstates,  $\psi_{i\alpha}^{\text{KS}}(\mathbf{r})$ , are then also eigenstates of  $\sigma_z$ , and are labeled according to the band index  $i$  and the spin index  $\alpha = 0, 1$ . The generalization of Eq. (8) to spin non-collinear cases requires the spin quantization axis not to be fixed along the z axis and to be free to rotate. In such a case, the spin density becomes a vector field

$$\mathbf{m}(\mathbf{r}) = \sum_i f_i \psi_i^{\text{KS}}(\mathbf{r})^\dagger \boldsymbol{\sigma} \psi_i^{\text{KS}}(\mathbf{r}). \quad (9)$$

Where the KS wave function is represented by a two-dimensional spinorial field. The spinor wave function is not an eigenstate of the  $\sigma_z$  Pauli matrix. This means that the spinor is not fully polarized, contrary to the eigenstates of ordinary spin DFT that are polarized either up or down (0, 1). The spinor state can be in a superposition of up and down spin states.

The spin non-collinear Hamiltonian can then be written as

$$\begin{aligned} \mathcal{H}_{\text{KS}}(\mathbf{r}) = & \left[ -\frac{1}{2}\nabla^2 + v_{\text{ext}}(\mathbf{r}) + v_{\text{H}}[n](\mathbf{r}) + \right. \\ & \left. + \bar{v}_{\text{xc}}^{\text{NC}}[n, \mathbf{m}](\mathbf{r}) \right] \mathbf{I}_2 + \mathbf{b}_{\text{s}}^{\text{NC}}[n, \mathbf{m}](\mathbf{r}) \cdot \boldsymbol{\sigma}, \quad (10) \end{aligned}$$

where

$$\mathbf{b}_{\text{s}}^{\text{NC}}[n, \mathbf{m}](\mathbf{r}) = \mu_{\text{B}} \mathbf{b}_{\text{ext}}(\mathbf{r}) + \mathbf{b}_{\text{xc}}^{\text{NC}}[n, \mathbf{m}](\mathbf{r}). \quad (11)$$

$\bar{v}_{\text{xc}}^{\text{NC}}[n, \mathbf{m}]$  and  $\mathbf{b}_{\text{xc}}^{\text{NC}}[n, \mathbf{m}]$  are functionals of the charge density and of the spin density vector fields and generalize  $\bar{v}_{\text{xc}}[n, m](\mathbf{r})$  and  $\mathbf{b}_{\text{xc}}[n, m](\mathbf{r})$  in the non-collinear case.

## 2.3 Time Dependent Density Functional Theory

As an extension of DFT to real time, TDDFT is based on the Runge-Gross theorem.<sup>44</sup> This

theorem states that if two external potentials,  $v_{\text{ext}}(\mathbf{r}, t)$  and  $v'_{\text{ext}}(\mathbf{r}, t)$ , both time-dependent and Taylor-expandable (around an initial time  $t_0$ ) differ by more than a simple time-dependent function  $C(t)$ , then the evolving time-dependent densities  $n(\mathbf{r}, t)$  and  $n'(\mathbf{r}, t)$  starting from the same ground state must also be different. This is equivalent to saying that there is always a one-to-one mapping between the external time-dependent potential and the electron density and to the observables. The van Leeuwen theorem guarantees instead that the time-dependent density  $n(\mathbf{r}, t)$  evolving from an initial state  $\Psi_0$  under an external potential  $v_{\text{ext}}(\mathbf{r}, t)$  can also be reproduced by a non-interacting system.<sup>45</sup>

The external potential can be expressed in the following general form

$$v_{\text{ext}}(\mathbf{r}, t) = v_{\text{ext}}^0(\mathbf{r}) + \theta(t - t_0) v_{\text{ext}}^1(\mathbf{r}, t). \quad (12)$$

Where  $v_{\text{ext}}^0(\mathbf{r})$  is the ground state external potential, corresponding to the bare electron-ion Coulomb interaction.  $v_{\text{ext}}^1(\mathbf{r}, t)$  is the external scalar time-dependent perturbation. The time-dependent KS equations are then written as<sup>46</sup>

$$\begin{aligned} i \frac{\partial}{\partial t} \psi_i^{\text{KS}}(\mathbf{r}, t) = & \left[ -\frac{1}{2}\nabla^2 + v_{\text{ext}}(\mathbf{r}, t) + v_{\text{H}}[n](\mathbf{r}, t) + \right. \\ & \left. + v_{\text{xc}}^{\text{NA}}[n, \Psi_0, \Phi_0](\mathbf{r}, t) \right] \psi_i^{\text{KS}}(\mathbf{r}, t), \quad (13) \end{aligned}$$

$v_{\text{xc}}^{\text{NA}}[n, \Psi_0, \Phi_0](\mathbf{r}, t)$  is the (non-adiabatic) exchange-correlation functional of the time-dependent density. This is also a functional of the initial many-body state  $\Psi_0$  and of the initial non-interacting KS state  $\Phi_0$ . In the case we start the evolution from the system's ground-state,  $\Psi_0$  and  $\Phi_0$  are both functionals of the initial density and  $v_{\text{xc}}^{\text{NA}}$  is simply a functional of the complete time-dependent density. The static exchange-correlation potential used to compute the ground-state electronic density must match the non-adiabatic exchange-correlation potential at time  $t = 0$ . However, at arbitrary times the two functionals do not

necessarily match

$$v_{\text{xc}}^{\text{NA}}[n](\mathbf{r}, t = 0) = v_{\text{xc}}[n](\mathbf{r}) . \quad (14)$$

The generalization of this formalism to spin-polarized systems produces the time-dependent extension of collinear spin DFT

$$i \frac{\partial \psi_{i\sigma}^{\text{KS}}(\mathbf{r}, t)}{\partial t} = \left[ \left( -\frac{1}{2} \nabla^2 + v_{\text{ext}}(\mathbf{r}, t) + v_{\text{H}}[n](\mathbf{r}, t) + \bar{v}_{\text{xc}}^{\text{NA}}[n, m](\mathbf{r}, t) \right) \mathbf{I}_2 + b_{\text{s}}^{\text{NA}}[n, m](\mathbf{r}, t) \sigma_z \right] \psi_{i\sigma}^{\text{KS}}(\mathbf{r}, t) . \quad (15)$$

Here,  $\sigma$  is the spin quantum number associated with the wave function.

## 2.4 The non-collinear spin TDDFT equations

The generalization to fully non-collinear systems is obtained by replacing the exchange-correlation functionals with their non-collinear extension

$$i \frac{\partial \psi_i^{\text{KS}}(\mathbf{r}, t)}{\partial t} = \left[ \left( -\frac{1}{2} \nabla^2 + v_{\text{ext}}(\mathbf{r}, t) + v_{\text{H}}[n](\mathbf{r}, t) + \bar{v}_{\text{xc}}^{\text{NA+NC}}[n, \mathbf{m}](\mathbf{r}, t) \right) \mathbf{I}_2 + \mathbf{b}_{\text{s}}^{\text{NA+NC}}[n, \mathbf{m}](\mathbf{r}, t) \cdot \boldsymbol{\sigma} \right] \psi_i^{\text{KS}}(\mathbf{r}, t) . \quad (16)$$

The effective magnetic field for the KS system is given by

$$\mathbf{b}_{\text{s}}^{\text{NA+NC}}[n, \mathbf{m}](\mathbf{r}, t) = \mathbf{b}_{\text{xc}}^{\text{NA+NC}}[n, \mathbf{m}](\mathbf{r}, t) + \mu_{\text{B}} \mathbf{b}_{\text{ext}}(\mathbf{r}, t) . \quad (17)$$

Under such time-dependent equations, the spin density satisfies the continuity equation,

$$\frac{d}{dt} \mathbf{m}(\mathbf{r}, t) = -\nabla \cdot \mathcal{J}_{\text{s}}(\mathbf{r}, t) + 2\mathbf{b}_{\text{s}}^{\text{NA+NC}}[n, \mathbf{m}](\mathbf{r}, t) \times \mathbf{m}(\mathbf{r}, t) , \quad (18)$$

where  $\mathcal{J}_{\text{s}}(\mathbf{r}, t)$  is the spin current of the KS system and the second term is a precessional contribution due to the coupling with the effective magnetic field. If we integrate over the entire volume of the system,  $\Omega$ , the first term ( $\nabla \cdot \mathcal{J}_{\text{s}}(\mathbf{r}, t)$ ) produces a surface term that is equal to zero, given that there is no loss of charge,

$$\frac{d\mathbf{M}_{\Omega}}{dt} = 2 \int_{\Omega} d\mathbf{r} \mathbf{b}_{\text{s}}^{\text{NA+NC}}[n, \mathbf{m}](\mathbf{r}, t) \times \mathbf{m}(\mathbf{r}, t) . \quad (19)$$

Eq. (19) gives the change in the total magnetization of the system over time. The contribution arising from the exchange-correlation magnetic field,  $\int_{\Omega} d\mathbf{r} \mathbf{b}_{\text{xc}}^{\text{NA+NC}}[n, \mathbf{m}](\mathbf{r}, t) \times \mathbf{m}(\mathbf{r}, t) = 0$ , due to the zero torque theorem.<sup>47,48</sup> In the presence of a homogeneous external magnetic field, the equation simply reduces to

$$\frac{d\mathbf{M}_{\Omega}}{dt} = 2\mu_{\text{B}} \mathbf{b}_{\text{ext}}(t) \times \mathbf{M}_{\Omega}(t) . \quad (20)$$

Eq. (20) describes a simple precession rotation around the axis of the externally applied magnetic field.

## 2.5 Approximations of the exchange correlation potential

Eq. (16) provides a formally exact spin  $\mathbf{m}(\mathbf{r}, t)$  and electronic density  $n(\mathbf{r}, t)$ 's evolution in external time-dependent fields. The key quantities are the two exchange correlation potentials  $\bar{v}_{\text{xc}}^{\text{NA+NC}}[n, \mathbf{m}]$  and  $\mathbf{b}_{\text{xc}}^{\text{NA+NC}}[n, \mathbf{m}]$ . These functionals are unknown in their exact form, and usually, two major approximations are used. The (i) adiabatic approximation; the (ii) locally collinear approximation. We briefly discuss these two approximations in the next subsections. Improvements beyond the adiabatic approximation have been discussed,<sup>49-59</sup> but we leave this for future implementations.

### The adiabatic approximation

The adiabatic approximation in TDDFT assumes that the functional dependence of the exchange-correlation potential at time  $t$  can be approximated only by the density at time  $t$ ,

which means that there is no memory and no dependence on the full electron density history. The nonadiabatic functional is then replaced by the functional of the ground-state DFT and used inside the time-dependent KS equations (13), (15) and (16) with instantaneous density and magnetization. In the non-collinear case, we can write

$$\begin{aligned} \bar{v}_{\text{xc}}^{\text{NA+NC}}[n, \mathbf{m}](\mathbf{r}, t) &\stackrel{\text{(A)}}{\simeq} \\ &\stackrel{\text{(A)}}{\simeq} \bar{v}_{\text{xc}}^{\text{GS+NC}}[n_0, \mathbf{m}_0](\mathbf{r}) \Big|_{\substack{n_0 \rightarrow n(\mathbf{r}, t) \\ \mathbf{m}_0 \rightarrow \mathbf{m}(\mathbf{r}, t)}} \end{aligned} \quad (21)$$

$$\begin{aligned} \mathbf{b}_{\text{xc}}^{\text{NA+NC}}[n, \mathbf{m}](\mathbf{r}, t) &\stackrel{\text{(A)}}{\simeq} \\ &\stackrel{\text{(A)}}{\simeq} \mathbf{b}_{\text{xc}}^{\text{GS+NC}}[n_0, \mathbf{m}_0](\mathbf{r}) \Big|_{\substack{n_0 \rightarrow n(\mathbf{r}, t) \\ \mathbf{m}_0 \rightarrow \mathbf{m}(\mathbf{r}, t)}} . \end{aligned} \quad (22)$$

Here,  $n_0$  and  $\mathbf{m}_0$  are the densities and magnetization of the electronic ground state. The adiabatic approximation is fully justified only when the external perturbation is slow enough to keep the physical system in its instantaneous eigenstate during evolution and neglect the memory dependence in the exchange-correlation functional. In linear response, this is equivalent to neglecting the frequency dependence in the exchange-correlation kernel.<sup>60</sup> This approximation is widely employed in TDDFT in the form of the so-called adiabatic local (spin) density approximation (AL(S)DA).<sup>61</sup>

$$\bar{v}_{\text{xc}}^{\text{ALDA+NC}}[n, \mathbf{m}](\mathbf{r}, t) = \frac{dE_{\text{xc}}^{\text{HEG}}[\bar{n}, \bar{\mathbf{m}}]}{d\bar{n}} \Big|_{\substack{\bar{n} \rightarrow n(\mathbf{r}, t) \\ \bar{\mathbf{m}} \rightarrow \mathbf{m}(\mathbf{r}, t)}} , \quad (23)$$

where  $E_{\text{xc}}^{\text{HEG}}[\bar{n}, \bar{\mathbf{m}}]$  is the exchange-correlation energy functional of the homogeneous electron gas. The value of the density  $\bar{n}$  at each point of the spatial grid is given by the density field  $n(\mathbf{r}, t)$ . The use of GGA functionals<sup>62</sup> would relax the locality in space condition by adding an additional dependence on the local gradient of the densities  $\nabla \bar{n}$  and  $\nabla \bar{\mathbf{m}}$ , but these will still be computed locally in space.

The exchange-correlation magnetic field, within

the AL(S)DA, is written as follows,

$$\mathbf{b}_{\text{xc}}^{\text{ALDA+NC}}[n, \mathbf{m}](\mathbf{r}, t) = \frac{dE_{\text{xc}}^{\text{HEG}}[\bar{n}, \bar{\mathbf{m}}]}{d\bar{\mathbf{m}}} \Big|_{\substack{\bar{n} \rightarrow n(\mathbf{r}, t) \\ \bar{\mathbf{m}} \rightarrow \mathbf{m}(\mathbf{r}, t)}} . \quad (24)$$

Limitations of such an approach have been discussed in the literature<sup>63,64</sup> and will not be analyzed further here.

## The locally collinear approximation

The functionals in Eq. (23) and (24) are functionals of both the electron density and the magnetization density vector<sup>48</sup> of the KS system. The locally collinear approximation employs widely used collinear functionals that depend only on the local spin-up ( $n_0$ ) and spin-down ( $n_1$ ) densities to approximate the full non-collinear functionals.<sup>65,66</sup>

In this approximation, the exchange-correlation energy functional of the non-collinear system is written as  $E_{\text{xc}}[n, \mathbf{m}] \stackrel{\text{(LC)}}{\simeq} E_{\text{xc}}^{\text{SDFT}}[n, |\mathbf{m}|]$ , where  $E_{\text{xc}}^{\text{SDFT}}$  is the exchange-correlation energy functional of the collinear SDFT. The exchange-correlation potentials in the locally-collinear approximation then become

$$\begin{aligned} \mathbf{b}_{\text{xc}}^{\text{ALDA+LC}}[n, \mathbf{m}](\mathbf{r}, t) &= \\ &= b_{\text{xc}}^{\text{ALDA}}[n, |\mathbf{m}|](\mathbf{r}, t) \cdot \frac{\mathbf{m}(\mathbf{r}, t)}{|\mathbf{m}(\mathbf{r}, t)|} \end{aligned} \quad (25)$$

$$\bar{v}_{\text{xc}}^{\text{ALDA+LC}}[n, \mathbf{m}](\mathbf{r}, t) = \bar{v}_{\text{xc}}^{\text{ALDA}}[n, |\mathbf{m}|](\mathbf{r}, t) . \quad (26)$$

Eq. (25) is ill-defined at  $\mathbf{m}(\mathbf{r}, t) = 0$ ; in this case, the exchange-correlation potential is also set to zero. Beyond this issue, the locally collinear functional has additional limitations:<sup>67</sup> (i) non-local functionals have an incorrect collinear limit; (ii) the locally collinear functionals are invariant under global rotation and satisfy the zero-torque theorem, but are insensitive to the local rotation of the magnetization vector; (iii) the locally collinear functionals have no well-defined functional derivatives.

Improvements on this approximation have been proposed,<sup>68</sup> existing local and non-local functionals have been modified to account for spin non-collinearity,<sup>69,70</sup> new gradient-corrected

functionals have been proposed based on the spin spiral state of the electron gas,<sup>71,72</sup> meta-GGA exchange-correlation functionals have been proposed.<sup>73,74</sup> We will not consider these functionals here; we will use locally collinear functionals in the simulations and focus on non-local functionals in a future study.

Under the locally collinear approximation and due to the zero local torque of the exchange-correlation field, the spin dynamics equation (18) becomes

$$\frac{d\mathbf{m}(\mathbf{r}, t)}{dt} = -\nabla \cdot \mathcal{J}_s(\mathbf{r}, t) + 2\mu_B \mathbf{b}_{\text{ext}}(\mathbf{r}, t) \times \mathbf{m}(\mathbf{r}, t), \quad (27)$$

which corresponds to the effective equation for the dynamics of the local magnetization vector.

## 2.6 Spin-orbit interaction and relativistic corrections

The Hamiltonian of non-collinear SDFE written in Eq. (10) is non-relativistic. Relativistic corrections are necessary for the description of the magnetic anisotropy and the interplay between spin and orbital degrees of freedom. A proper discussion of the origin of the spin-orbit interaction, starting from fundamental quantum mechanical principles, would require us to start from the full Dirac equation<sup>75</sup> and go beyond the scope of this work. Recent works implement full relativistic TDDFT<sup>76</sup> and apply four-current TDDFT to the study of chiral induced spin selectivity.<sup>77</sup>

Here we consider the semi-relativistic Hamiltonian obtained from the expansion of the Dirac equation to the order  $O(1/(mc)^2)$  for a single electron in the presence of KS potential  $v_{\text{KS}}[n](\mathbf{r})$ . The relativistic electron equation is written as

$$i\partial_t \Psi^{\text{KS}} = [-i\alpha^k \partial_k + \beta mc^2 + v_{\text{KS}}[n](\mathbf{r}, t)] \Psi^{\text{KS}}, \quad (28)$$

$\Psi^{\text{KS}}$  is a four-dimensional spinor,  $\alpha^k$  and  $\beta$  are the Dirac matrices.  $\Psi^{\text{KS}}$  can be separated into a small and a large component  $\Psi_S^{\text{KS}}$  and  $\Psi_L^{\text{KS}}$ . For applications in solid state and molecular physics, the small component is neglected and

the equation for the large component is written as<sup>78</sup>

$$\left\{ \frac{\mathbf{p}^2}{2} + v_{\text{KS}}[n](\mathbf{r}) - \frac{\mathbf{p}^4}{8c^2} + \frac{\nabla^2 v_{\text{KS}}[n](\mathbf{r})}{8c^2} + \frac{1}{4c^2} (\nabla v_{\text{KS}}[n](\mathbf{r}) \times \mathbf{p}) \cdot \boldsymbol{\sigma} \right\} \tilde{\Psi}_L^{\text{KS}} = E_{(\text{SR})}^{\text{KS}} \tilde{\Psi}_L^{\text{KS}}. \quad (29)$$

The third term in the semi-relativistic Hamiltonian is a relativistic kinetic correction, the fourth term is the Darwin interaction, which is a relativistic correction that becomes more important close to the nuclei, and the last term is the spin-orbit interaction. The spin-orbit interaction is dependent on the effective electrostatic potential experienced by the electrons. In the KS system, this corresponds to the effective KS scalar potential acting on each electron. The spin-orbit interaction can be rearranged as follows,

$$\begin{aligned} V_{\text{SO}} &= \frac{1}{4c^2} (\nabla v_{\text{KS}}[n](\mathbf{r}) \times \mathbf{p}) \cdot \boldsymbol{\sigma} \\ &= \frac{1}{4c^2} (\nabla v_{\text{ext}}(\mathbf{r}) \times \mathbf{p}) \cdot \boldsymbol{\sigma} + \\ &+ \frac{1}{4c^2} (\nabla v_{\text{Hxc}}[n](\mathbf{r}) \times \mathbf{p}) \cdot \boldsymbol{\sigma}. \end{aligned} \quad (30)$$

The first contribution is due to the bare ionic external potential, and the second is the mean-field part due to the electrostatic cloud formed by the other electrons in the system. Here  $n = n_C + n_V$  is the total system's electron density given by the sum of the core and valence densities. We could separate the effect of the core from the valence electrons in Eq. (30).

$$\begin{aligned} V_{\text{SO}} &= \frac{1}{4c^2} (\nabla \tilde{v}[n_C](\mathbf{r}) \times \mathbf{p}) \cdot \boldsymbol{\sigma} + \\ &+ \frac{1}{4c^2} (\nabla \delta v_{\text{Hxc}}[n_C, n_V](\mathbf{r}) \times \mathbf{p}) \cdot \boldsymbol{\sigma}, \end{aligned} \quad (31)$$

where we have introduced the following effective potentials,

$$\tilde{v}[n_C](\mathbf{r}) = v_{\text{ext}}(\mathbf{r}) + v_{\text{Hxc}}[n_C, 0](\mathbf{r}), \quad (32)$$

$$\begin{aligned} \delta v_{\text{Hxc}}[n_C, n_V](\mathbf{r}) &= \\ &= v_{\text{Hxc}}[n_C, n_V](\mathbf{r}) - v_{\text{Hxc}}[n_C, 0](\mathbf{r}). \end{aligned} \quad (33)$$

The first term in  $V_{\text{SO}}$  is the most important one and corresponds to the spin-orbit coupling due to the combined effect of the bare ionic potential and the electronic charge of the core electrons. Due to the localization of the core electron charge, it can be written as a linear combination of effective potentials centered around the nuclei

$$\tilde{v}[n_{\text{C}}](\mathbf{r}) = \sum_{\text{a}=1}^{N_{\text{a}}} \tilde{v}^{\text{a}}[n_{\text{C}}^{\text{a}}](\mathbf{r} - \mathbf{R}_{\text{a}}) \quad (34)$$

$\delta v_{\text{Hxc}}(\mathbf{r})$  is the electrostatic potential due to the remaining valence charge and is usually neglected in calculations.

The effective potential,  $\tilde{v}[n_{\text{C}}](\mathbf{r})$ , is often approximated in the KS equations by using a pseudo-potential,  $v_{\text{ps}}(\mathbf{r})$ , centered on every atom. We discuss this in more detail in the implementation section. In the case of a single atom  $v_{\text{ext}}(\mathbf{r}) = -\frac{Z}{r}$  and if we neglect the effect of other electrons, we recover the ordinary form of the spin-orbit interaction

$$V_{\text{SO}} = \frac{Z}{4c^2 r^3} (\mathbf{r} \times \mathbf{p}) \cdot \boldsymbol{\sigma} = \lambda \mathbf{L} \cdot \boldsymbol{\sigma}, \quad (35)$$

with  $\lambda = \frac{Z}{4c^2 r^3}$ .

The spin continuity equation (27) should be rewritten as

$$\frac{d\mathbf{m}(\mathbf{r}, t)}{dt} = -\nabla \cdot \mathcal{J}_{\text{s}}(\mathbf{r}, t) + 2\mu_{\text{B}} \mathbf{b}_{\text{ext}}(\mathbf{r}, t) \times \mathbf{m}(\mathbf{r}, t) + \boldsymbol{\Gamma}_{\text{SOC}}(\mathbf{r}, t), \quad (36)$$

where  $\boldsymbol{\Gamma}_{\text{SOC}}(\mathbf{r}, t)$  defines an additional spin-orbit torque term.

### 3 Numerical Implementation

In this section, we discuss the details of the implementation of the spin non-collinear formalism in INQ.

#### 3.1 Spinorial representation

The single-particle wavefunctions of the non-collinear spin KS Hamiltonian (10) are in spinor

form. Spinors are two-dimensional vectors that transform according to the  $\text{SU}(2)$  representation of the three-dimensional rotation group.

$$\psi_{\text{i}}^{\text{KS}}(\mathbf{r}) \rightarrow e^{i\frac{\phi}{2}(\hat{\mathbf{n}} \cdot \hat{\boldsymbol{\sigma}})} \psi_{\text{i}}^{\text{KS}}(\mathbf{r}) \quad (37)$$

In practice, this means we need to include an additional index in the representations of the orbitals that also have indices for the states and basis coefficients.

We have found that to obtain the most efficient memory layout, it is better to have the spinor index in the middle of the array, in between the basis coefficient and orbital indices. In this way, there are three possible views of the wave-function array. The first one is to have the spinor index explicitly, for operations that involve spinor components like application to the potential or the calculation of the spin density. The second view is a 2-dimensional array obtained by flattening the spinor and orbital indices to effectively duplicate the number of states. This view is useful for operations that act individually on each state and do not involve spinor information, like the calculation of the Laplacian. Finally, we can obtain a different 2-dimensional view of the array by compacting the basis coefficient and spinor indices. In this case we can think that the spinor dimension duplicates the size of the basis coefficients. These means that operations like orthogonalization can be easily done using the same code as the collinear case. All these different views are managed by the Multi<sup>?</sup> library without any copies of access overhead.

In the spinorial representation, it is convenient to introduce the KS spin density matrix  $\rho_{\text{s}}^{\text{KS}}(\mathbf{r})$ .

$$\begin{aligned} \rho_{\text{s}}^{\text{KS}}(\mathbf{r}) &= \begin{bmatrix} \sum_{\text{i}} f_{\text{i}} \psi_{\text{i}\uparrow}^{\text{KS}}(\mathbf{r}) \psi_{\text{i}\uparrow}^{\text{KS}}(\mathbf{r})^* & \sum_{\text{i}} f_{\text{i}} \psi_{\text{i}\uparrow}^{\text{KS}}(\mathbf{r}) \psi_{\text{i}\downarrow}^{\text{KS}}(\mathbf{r})^* \\ \sum_{\text{i}} f_{\text{i}} \psi_{\text{i}\downarrow}^{\text{KS}}(\mathbf{r}) \psi_{\text{i}\uparrow}^{\text{KS}}(\mathbf{r})^* & \sum_{\text{i}} f_{\text{i}} \psi_{\text{i}\downarrow}^{\text{KS}}(\mathbf{r}) \psi_{\text{i}\downarrow}^{\text{KS}}(\mathbf{r})^* \end{bmatrix} = \\ &= \begin{bmatrix} \rho_{\text{s}}^{\uparrow\uparrow}(\mathbf{r}) & \rho_{\text{s}}^{\uparrow\downarrow}(\mathbf{r}) \\ \rho_{\text{s}}^{\downarrow\uparrow}(\mathbf{r}) & \rho_{\text{s}}^{\downarrow\downarrow}(\mathbf{r}) \end{bmatrix} \end{aligned} \quad (38)$$

From  $\rho_{\text{s}}^{\text{KS}}(\mathbf{r})$  the magnetization density is sim-

ply given by

$$\mathbf{m}(\mathbf{r}) = \text{Tr}[\hat{\sigma}\rho_s^{\text{KS}}(\mathbf{r})] \quad (39)$$

and reduces to the different components;

$$m_x(\mathbf{r}) = \rho_s^{\uparrow\downarrow}(\mathbf{r}) + \rho_s^{\downarrow\uparrow}(\mathbf{r}) = 2\text{Re}[\rho_s^{\uparrow\downarrow}(\mathbf{r})] \quad (40)$$

$$m_y(\mathbf{r}) = i(\rho_s^{\uparrow\downarrow}(\mathbf{r}) - \rho_s^{\downarrow\uparrow}(\mathbf{r})) = -2\text{Im}[\rho_s^{\uparrow\downarrow}(\mathbf{r})] \quad (41)$$

$$m_z(\mathbf{r}) = \rho_s^{\uparrow\uparrow}(\mathbf{r}) - \rho_s^{\downarrow\downarrow}(\mathbf{r}) \quad (42)$$

In the code, we store the spin-density matrix  $\rho_v(\mathbf{r})$  as a four-dimensional vector of real values

$$\rho_v(\mathbf{r}) = [\rho_s^{\uparrow\uparrow}(\mathbf{r}), \rho_s^{\downarrow\downarrow}(\mathbf{r}), \text{Re}[\rho_s^{\uparrow\downarrow}(\mathbf{r})], \text{Im}[\rho_s^{\uparrow\downarrow}(\mathbf{r})]] . \quad (43)$$

This is more efficient than storing the full complex matrix that has redundant values due to its hermiticity. The conversion between  $\rho_v(\mathbf{r})$  and the magnetization density  $\mathbf{m}(\mathbf{r})$  is straightforward through Eqs. (40), (41) and (42).

### 3.2 Local moments initialization procedure

The electron density can be initialized from a linear combination of atomic densities directly on the real-space grid. In the case of spin-polarized and non-collinear systems, we must initialize the full spin density matrix  $\rho_s(\mathbf{r})$ . The initial guess for the spin density matrix of the system can be written as follows.

$$\rho_s(\mathbf{r}) = \sum_{a=1}^{N_a} \rho_s^a(\mathbf{r} - \mathbf{R}_a) \quad (44)$$

$\rho_s^a(\mathbf{r} - \mathbf{R}_a)$  is the atomic density matrix centered around the atom  $a$  and it is obtained from the charge distribution,  $n_a(|\mathbf{r}|)$ , normally extracted from the pseudo-potential file, and from the initial atomic magnetic moment,  $\mathbf{m}_a$ , which must be provided in input.

At each point  $\mathbf{r}$  on the spatial grid, the initial guess for the spin density matrix is calculated according to the pseudo-algorithm in Fig. (1) and stored in the vector field variable  $\rho_v(\mathbf{r})$ , a field set defined on the spatial grid.

### 3.3 The exchange correlation potential in spinorial representation

Within the adiabatic and locally collinear approximation in Eq. (25) and Eq. (26), the exchange-correlation potential can be expressed as

$$\mathcal{V}_{\text{xc}}[n, \mathbf{m}](\mathbf{r}, t) = \bar{v}_{\text{xc}}^{\text{LC+ALDA}}[n, \mathbf{m}](\mathbf{r}, t)\mathbf{I}_2 + \mathbf{b}_{\text{xc}}^{\text{LC+ALDA}}[n, \mathbf{m}](\mathbf{r}, t) \cdot \boldsymbol{\sigma} \quad (45)$$

By omitting the labels, this is equivalent in spinorial representation to

$$\hat{\mathcal{V}}_{\text{xc}} = \begin{bmatrix} \bar{v}_{\text{xc}} + b_{\text{xc}}^z & b_{\text{xc}}^- \\ b_{\text{xc}}^+ & \bar{v}_{\text{xc}} - b_{\text{xc}}^z \end{bmatrix}$$

where we have used  $b_{\text{xc}}^{\pm} = b_{\text{xc}}^x \pm ib_{\text{xc}}^y$ . This leads to the following expression for the exchange-correlation energy (at a given time).

$$\begin{aligned} E_{\text{xc}} &= \int_{\Omega} d\mathbf{r} \text{Tr}[\hat{\mathcal{V}}_{\text{xc}}(\mathbf{r})\hat{\rho}_s^{\text{KS}}(\mathbf{r})] \\ &= \int_{\Omega} d\mathbf{r} [\rho_s^{\uparrow\uparrow}(\mathbf{r})(\bar{v}_{\text{xc}}(\mathbf{r}) + b_{\text{xc}}^z(\mathbf{r})) + \\ &\quad + \rho_s^{\downarrow\downarrow}(\mathbf{r})(\bar{v}_{\text{xc}}(\mathbf{r}) - b_{\text{xc}}^z(\mathbf{r})) + 2\text{Re}[\rho_s^{\uparrow\downarrow}(\mathbf{r})]b_{\text{xc}}^x(\mathbf{r}) - \\ &\quad - 2\text{Im}[\rho_s^{\uparrow\downarrow}(\mathbf{r})]b_{\text{xc}}^y(\mathbf{r})] \\ &= \langle \rho_v, \mathcal{V}_v^{\text{xc}} \rangle \end{aligned} \quad (46)$$

$\mathcal{V}_v^{\text{xc}}(\mathbf{r})$  is the four-dimensional vectorial representation of the exchange-correlation field

$$\begin{aligned} \mathcal{V}_v^{\text{xc}}(\mathbf{r}) &= [\bar{v}_{\text{xc}}^+(\mathbf{r}), \bar{v}_{\text{xc}}^-(\mathbf{r}), 2b_{\text{xc}}^x(\mathbf{r}), -2b_{\text{xc}}^y(\mathbf{r})] \\ \bar{v}_{\text{xc}}^+(\mathbf{r}) &= \bar{v}_{\text{xc}}(\mathbf{r}) + b_{\text{xc}}^z(\mathbf{r}) \\ \bar{v}_{\text{xc}}^-(\mathbf{r}) &= \bar{v}_{\text{xc}}(\mathbf{r}) - b_{\text{xc}}^z(\mathbf{r}), \end{aligned} \quad (47)$$

and  $\langle \mathbf{v}, \mathbf{u} \rangle$  is the Cartesian scalar product between the two vectors  $\mathbf{v}$  and  $\mathbf{u}$ .

### 3.4 Zeeman coupling and external magnetic field

Analogously to the exchange-correlation magnetic field, the Zeeman coupling to an external homogeneous magnetic field,  $\mathbf{b}_{\text{ext}} = [b_{\text{ext}}^x, b_{\text{ext}}^y, b_{\text{ext}}^z]$ , is also defined in the spinorial

Figure 1: Spin Density Matrix Initialization

```

1: procedure   DMINITIALIZATION(Spacegrid,   AtomsList,
   MagneticMoments)
2:   function NEARESTATOM(i,Spacegrid,AtomsList)
3:      $r \leftarrow \text{Spacegrid}[i]$ 
4:      $a \leftarrow \text{VORONOI}(r, \text{AtomsList})$ 
5:     return a
6:   end function
7:   function COMPUTESPINDENSITY(M,n)
8:      $\rho_v \leftarrow [0, 0, 0, 0]$ 
9:     if  $n > 0$  then
10:       $m \leftarrow M/n; \quad \rho_v \leftarrow [(1 + m[2])/2, (1 -$ 
    $m[2])/2, m[0]/2, -m[1]/2]$ 
11:     end if
12:     return  $n\rho_v$ 
13:   end function
14:    $i \leftarrow 0; N \leftarrow \text{len}(\text{spacegrid})$ 
15:   for  $i \in 0 \dots N - 1$  do
16:      $a \leftarrow \text{NEARESTATOM}(i, \text{SpaceGrid}, \text{AtomsList})$ 
17:      $d \leftarrow \text{DISTANCE}(\text{Spacegrid}[i], \text{Spacegrid}[\text{R}(a)])$ 
18:      $\rho_v[i] \leftarrow \text{COMPUTESPINDENSITY}(\text{MagneticMoments}[a],$ 
    $\text{Density}[a](d))$ 
19:   end for
20:   return  $\rho_v$ 
21: end procedure

```

representation using

$$\hat{V}_z = \mu_B \boldsymbol{\sigma} \cdot \mathbf{b}_{\text{ext}} = \mu_B \begin{bmatrix} b_{\text{ext}}^z & b_{\text{ext}}^- \\ b_{\text{ext}}^+ & -b_{\text{ext}}^z \end{bmatrix}$$

where  $b_{\text{ext}}^- = b_{\text{ext}}^x - ib_{\text{ext}}^y$  and  $b_{\text{ext}}^+ = b_{\text{ext}}^x + ib_{\text{ext}}^y$ . In the collinear case, the two off-diagonal terms disappear, and the expression reduces to a fully diagonal form.

The Zeeman energy is computed as the exchange-correlation energy using  $\langle \rho_v, \mathcal{V}_v^z \rangle$ . We only implemented the spin Zeeman term here; we will leave the orbital Zeeman contribution or orbital response to an external magnetic field<sup>79</sup> for a future study.

### 3.5 Spin-orbit coupling implementation

Here we discuss the implementation of the spin-orbit interaction based on the pseudopotential method. Other implementations are available in the literature based on the first-order perturbation theory variation of scalar relativistic wave functions,<sup>80,81</sup> but will not be considered here. A fully relativistic treatment of the problem would require a four-component formalism based on Dirac spinors,<sup>82</sup> as discussed in the theory section. We have also seen that all relativistic effects up to order  $\alpha^2$  (where  $\alpha$  is the fine structure constant) can be captured from a Schrödinger-like equation with an additional spin-orbit term.<sup>83,84</sup> In this form, the total ionic pseudopotential can be written as

$$\hat{v}_{\text{ps}} = \sum_{a=1}^{N_a} \left\{ \hat{V}_L^a + \sum_{l,j,m_j} \frac{|\delta V_{lj}^a \phi_{lj;m_j}^a\rangle \langle \phi_{lj;m_j}^a| \delta V_{lj}^a|}{\langle \phi_{lj;m_j}^a | \delta V_{lj}^a | \phi_{lj;m_j}^a \rangle} \right\} \quad (48)$$

The contribution  $\hat{V}_L^a$  is local in space and long-range. The second term in the sum over the atoms is the short-range non-local atomic contribution. The set of wave functions  $\{\phi_{lj;m_j}^a\}$  corresponds to the solution of the KS problem for the isolated atom (indicated with the label  $a$ ). These are expressed as the product of a radial component and of the spinorial spherical

harmonics.

$$\begin{aligned} |\phi_{lj;m_j}^a\rangle &= |R_{lj}^a\rangle \otimes |\Phi_{lj}^{m_j}\rangle \\ \langle \mathbf{r} | \phi_{lj;m_j}^a \rangle &= R_{lj}^a(|\mathbf{r} - \mathbf{R}_a|) \Phi_{lj}^{m_j}(\hat{\Omega}) \end{aligned} \quad (49)$$

The first factor of the atomic pseudo wave function is the radial component,  $R_{lj}^a$ , and the second factor is the spinorial spherical harmonics

$$\begin{aligned} \Phi_{l,j=l\pm\frac{1}{2}}^{m_j=m\pm\frac{1}{2}}(\hat{\Omega}) &= \sqrt{\frac{l\pm m+1}{2l+1}} \Upsilon_l^{m_j-\frac{1}{2}}(\hat{\Omega}) \chi_{\uparrow\pm} \\ &\pm \sqrt{\frac{l\mp m}{2l+1}} \Upsilon_l^{m_j+\frac{1}{2}}(\hat{\Omega}) \chi_{\downarrow}. \end{aligned} \quad (50)$$

The potential  $\delta V_{lj}(\mathbf{r})^a = V_{lj}^a(\mathbf{r} - \mathbf{R}_a) - V_L^a(\mathbf{r} - \mathbf{R}_a)$  is the difference between the pseudo-potential channel  $(l, j)$  and the local long-range pseudo-potential  $V_L^a$ . In the next section, we discuss simulations of different systems using this spin non-collinear implementation for both ground state DFT and real-time TDDFT.

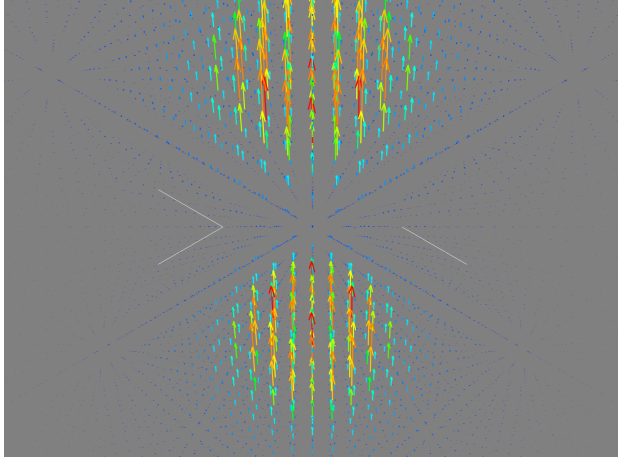
## 4 Results and discussion

This section is organized as follows. We first discuss the spin density texture and the spin non-collinearity in magnetic clusters and solids. Then we look at the spin-orbit and Zeeman splitting in the presence of external magnetic fields in atoms and the magnetic response of paramagnetic solids. Finally, we focus on the real-time dynamics of magnetic systems under external magnetic and electric pulses.

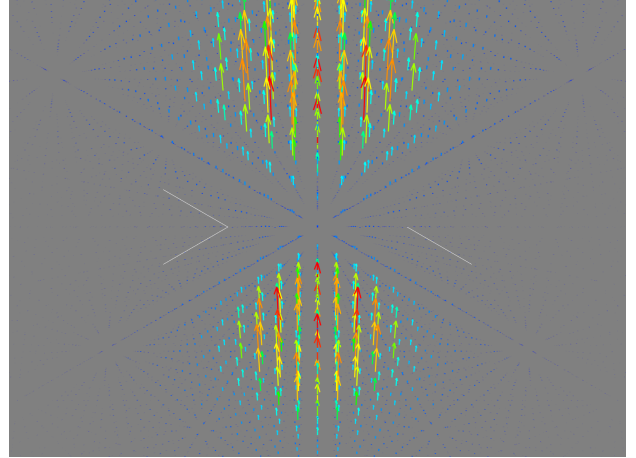
### 4.1 Spin non-collinearity in magnetic clusters

We tested the non-collinear spin implementation by computing the electronic ground state of different magnetic clusters.

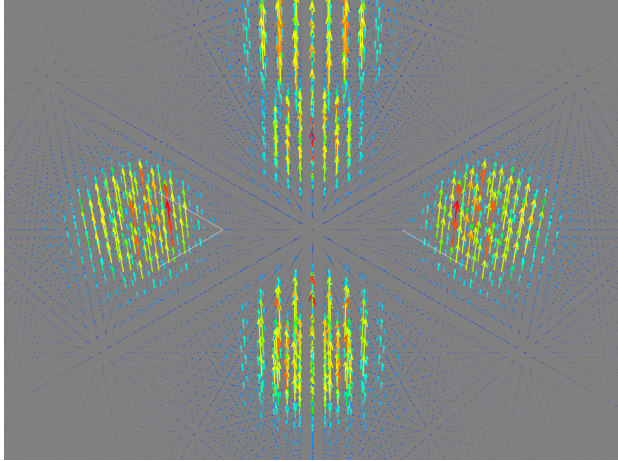
In Fig. (2) we show the magnetization density field of the  $\text{Fe}_2$  magnetic cluster. The distance between the Fe atoms is  $1.99 \text{ \AA}$ . The calculation is performed in a cubic box of size  $15 \text{ \AA}$  to ensure that the cluster is isolated. We include the spin-orbit interaction using full-relativistic pseudo-potentials. The total magnetic moment of the  $\text{Fe}_2$  cluster is in agreement with pre-



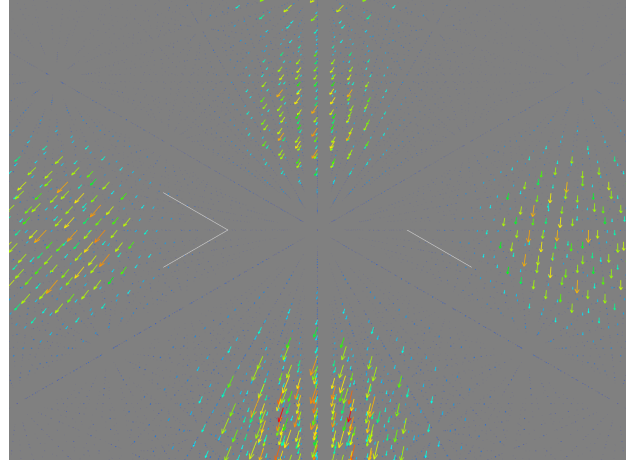
(a)  $\text{Fe}_2$  spin density field



(b)  $\text{Fe}_2$  with spin-orbit interaction



(c)  $\text{Fe}_6$  spin density field



(d)  $\text{Fe}_6$  non-collinear spin density field

Figure 2: Spin density profile of non-collinear magnetic Fe clusters. In panel (a) and (b) we show the spin density profile for the  $\text{Fe}_2$  cluster. Panel (a) without spin-orbit interaction and panel (b) with spin-orbit interaction. The degree of spin non-collinearity induced by spin-orbit is small and the two calculations produce very similar spin density profiles. In panel (c) and (d) we instead consider the  $\text{Fe}_6$  cluster. In panel (d) we consider the full spin density profile  $(m_x, m_y, m_z)$ . In panel (d) we instead remove the z-component and show  $(m_x, m_y, 0)$  to emphasize the importance of the spin non-collinearity for the description of the magnetic cluster.

vious results and calculations using different codes. The magnetic moment along the z-axis is  $M_z = 6.12\mu_B$ . Calculations with and without spin-orbit interaction produce a negligible difference in spin texture, as can be seen from Figs. (2(a)) and (2(b)). The arrows in the figure point along the direction of magnetization at each point in the spatial grid. It is easy to observe that at each point the spin density is approximately oriented along the z-axis, producing a total net magnetic moment oriented along the z-axis. The magnetic structure of the  $\text{Fe}_6$  cluster is more complex. The optimized geometry of the cluster and its magnetic structure is consistent with previous works.<sup>85</sup> The magnetic moment of the system is approximately oriented along the z-axis with magnitude  $M_z = 19.98\mu_B$ ; in addition, it has small but not negligible  $x$  and  $y$  components ( $M_x = 0.71\mu_B$ ,  $M_y = 0.40\mu_B$ ). This is reflected in a magnetic texture characterized by a higher degree of non-collinearity compared to the  $\text{Fe}_2$  case. In Fig. (2(c)) we show the complete spin density profile of the system. This is compared in panel (d) of the same figure, which shows only the  $x$  and  $y$  components of the spin density obtained after removing the dominant  $z$  component. Although much smaller in magnitude, this non-collinear contribution is clearly not negligible, as can be seen from Fig. (2(d)), and must be accounted for in a complete description of the magnetism of the cluster.

## 4.2 Spin non-collinear calculation of magnetically ordered solids

Table 1: Comparison of the magnetic moment calculated by INQ and Quantum Espresso for different ferromagnetic solids.

Ferromagnet	Magnetic moment [ $\mu_B$ ]	
	INQ	Quantum Espresso
bcc Fe	2.2208	2.2210
fcc Ni	0.6379	0.6365
fcc Co	1.6362	1.6367

In Table (1) we show the computed magnetic moments of three metallic ferromagnets; bcc Fe, fcc Ni and fcc Co. The calculations were performed using the LDA exchange-correlation functional and compared with analogous calculations from **Quantum Espresso (QE)**.<sup>86</sup> The PBE functional produces only minor changes to the final magnetic moments in comparison to the results obtained using LDA. We use a  $\mathbf{k}$ -points grid of size  $13 \times 13 \times 13$  and include 20 empty bands to reach convergence in INQ. We also used a Fermi-Dirac smearing with a fictitious temperature of  $300\text{ K}$  to compute the occupations of the electronic states. We initialized the magnetic moments following the procedure discussed in Algorithm (1). In comparison to the  $\text{Fe}_6$  cluster, here the degree of non-collinearity is much lower with the magnetic moments fully oriented along the z-axis. The comparison with the results from QE is quite accurate, and we did not observe sensible variations in the values of the magnetic moments and ground-state energies.

## 4.3 Spin-orbit coupling induced energy splittings

Table 2: Energy levels splitting with fully relativistic pseudopotentials for different atoms.

Element	Orbital	Level splitting [Ha]	
		INQ	Quantum Espresso
Xe	5p	0.0453	0.0464
Au	5d	0.0045	0.0045
Pb	5d	0.0002	0.0003
Ag	5d	0.0030	0.0032

In atoms, the splitting of the energy levels due to spin-orbit coupling is similar in size to the relativistic corrections to the kinetic energy and the Zitterbewegung effect,<sup>87</sup> therefore it cannot be neglected. These corrections contribute to the fine structure of the atom. In Table (2) we look at the fine structure of the atomic energy levels induced by the fully relativistic pseudopotentials.  $\Delta E(5p)$  for Xe is the intra-level splitting due to spin-orbit interaction of the  $5p$  states. For the other elements, we instead con-

sider the intra-level splitting of the lowest energy  $5d$  degenerate states. Calculations were performed for the isolated atoms shown in the Table (2), using the local collinear approximation of LSDA for the exchange-correlation functional. We use fully relativistic pseudopotentials from the *PseudoDojo* library.<sup>88</sup> The calculations are then compared with analogous simulations performed using QE<sup>86</sup> and the results appear in good agreement. As already discussed, the pseudopotential approximation in the case of spin-orbit coupling consists of removing the contribution of the valence electrons to the effective electric field  $\nabla v_{\text{KS}}$  generated by the KS potential in Eq. (30). This is often considered a good approximation for the electrons close to the nuclei that experience an electric field mainly determined by the electrostatic bare nuclear potential and the interaction with the core electrons. In the next section, we analyze the magnetic response to an applied external magnetic field.

#### 4.4 Calculation of Zeeman splittings

Table 3: Energy level splitting in the H atom  $1s$  levels as a function of the applied magnetic field. The results are compared with calculations from VASP<sup>89,90</sup>

$b_{\text{ext}}^z$ [eV]	$\Delta E_Z$ [eV]	
	INQ	VASP
0.1	0.1997	0.2000
0.3	0.5993	0.6000
0.5	0.9988	1.0000
0.7	1.3984	1.4000
1.0	1.9977	2.0000

In this section, we discuss the calculation of the Zeeman energy splitting in the case of a few simple atoms and compare the results with analogous calculations performed using the VASP code.<sup>91</sup> In Tables (3) and (4) we look

Table 4: Energy level splitting in the Al atom  $3s$  levels as a function of the applied magnetic field. The results are compared with calculations from VASP<sup>89,90</sup>

$b_{\text{ext}}^z$ [eV]	$\Delta E_Z$ [eV]	
	INQ	VASP
0.1	0.2025	0.1998
0.3	0.6024	0.5998
0.5	1.0019	0.9998
0.7	1.4015	1.3998
1.0	2.0008	1.9998

at the energy splitting under an applied external magnetic field of the  $1s$  energy levels in H and the  $3s$  levels of Al.

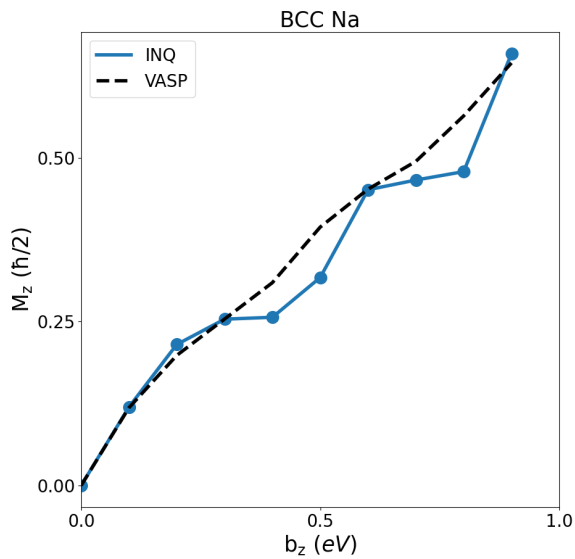
The simulations are performed by applying an external magnetic field of magnitude in eV given in the first column of the table along the  $z$ -axis. The simulation is performed in INQ using the non-collinear implementation, but the same results are obtained also using the standard collinear implementation. The results agree well with the two codes and are easy to understand from the expression of the Zeeman coupling. In this case, we will have the following expression for the Zeeman potential.

$$\hat{V}_z = \mu_B \sigma_z \cdot b_{\text{ext}}^z = \mu_B \begin{bmatrix} b_{\text{ext}}^z & 0 \\ 0 & -b_{\text{ext}}^z \end{bmatrix}$$

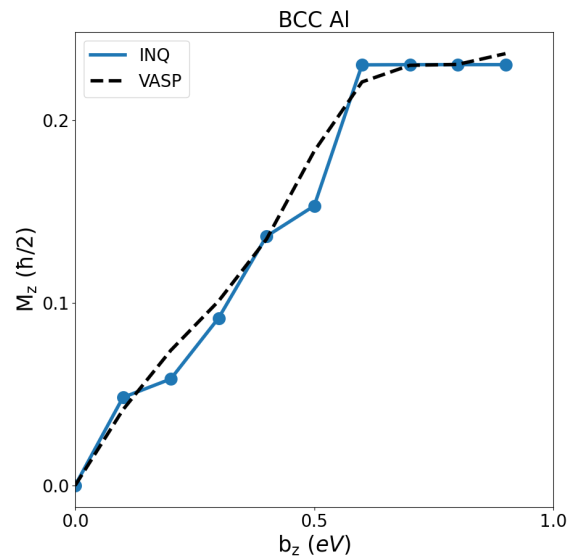
This term breaks the degeneracy in the spin space, producing different energies for the spin up- and down- states  $s = \pm 1$ ,  $E_z^s = s b_{\text{ext}}^z$  [eV]. The Zeeman splitting energy is given by  $\Delta E_z = 2 b_{\text{ext}}^z$  [eV], which is consistent with the values in the Tables (3) and (4) for H and Al, respectively.

#### 4.5 Calculation of Zeeman response

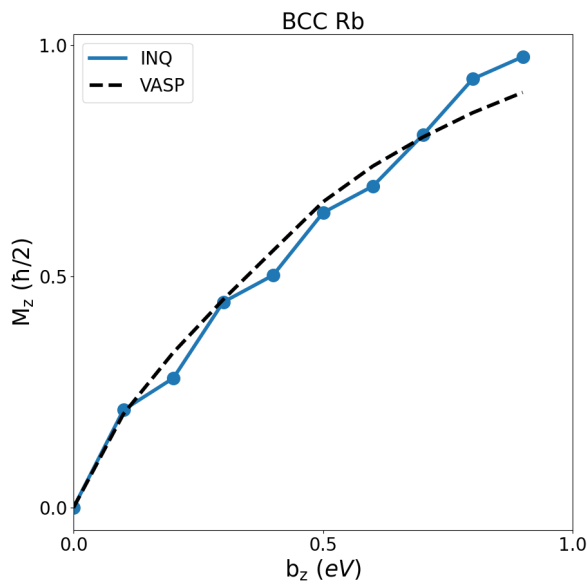
The magnetic susceptibility of conduction electrons in metals consists of two contributions.



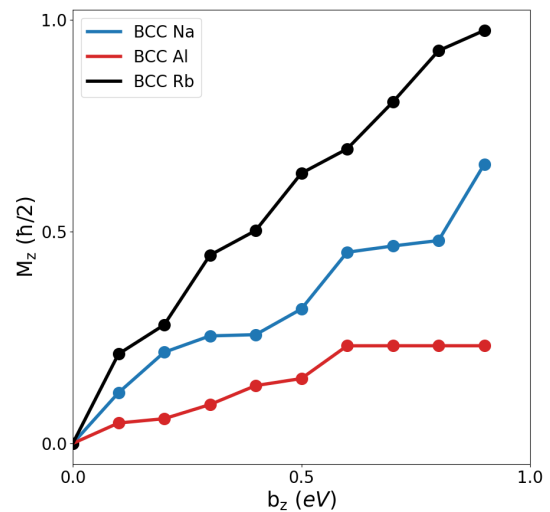
(a) Comparison between INQ and VASP magnetic moments response in BCC Na.



(b) Comparison between INQ and VASP magnetic moments response in BCC Al.



(c) Comparison between INQ and VASP magnetic moments response in BCC Rb.



(d) Magnetic moments of paramagnetic metals as a function of magnetic field strength.

Figure 3: Magnetic moment response under externally applied magnetic fields in paramagnetic metal solids.

The first,  $\chi_P$ , comes from the spin magnetic moment response under the application of an external magnetic field,<sup>92</sup> the second is the diamagnetic orbital response to an applied external magnetic field.

Here we consider Pauli paramagnetism that arises from the Zeeman coupling between the electron spin and the externally applied magnetic field. In Fig. (3) we show the comparison in the magnetic moment response under externally applied magnetic fields of different strengths in the case of three different paramagnetic metals, BCC Na (panel a), BCC Al (panel b) and BCC Rb (panel c).

The results are compared with calculations performed with VASP. In both cases, we used a local-collinear LDA functional and a  $8 \times 8 \times 8$   $\mathbf{k}$ -points grid to compute the electronic ground state in the presence of the applied magnetic field. The external magnetic field,  $\mathbf{b}_{\text{ext}}$ , is spatially homogeneous and oriented along the  $z$ -axis. The results appear to be independent of the choice of the exchange-correlation functional and appear to be in good agreement between two codes. In the case of Rb, there is a steady increase in the magnetic moment as a function of the applied field with a higher slope compared to the other two metals Al and Na (panel (d) of the figure) which is associated with a higher magnetic susceptibility.

## 4.6 Real time dynamics under applied magnetic fields

### 4.6.1 single atom dynamics

In Fig. (4) we look at the dynamics of a single H atom with the initial magnetic moment oriented along the  $z$ -axis.

In the absence of spin-orbit interaction, the spin continuity equation (18) can be simplified further given that the effect of the spin currents is negligible in a single isolated atom. The exchange-correlation magnetic field for a spin-polarized hydrogen atom sums up to the applied external magnetic field ( $B = 1$  is in atomic units and corresponds to 0.5 Ha of Zeeman energy). The equation reduces to Eq. (19), but now the magnetization field  $\mathbf{m}(\mathbf{r}, t)$  is com-

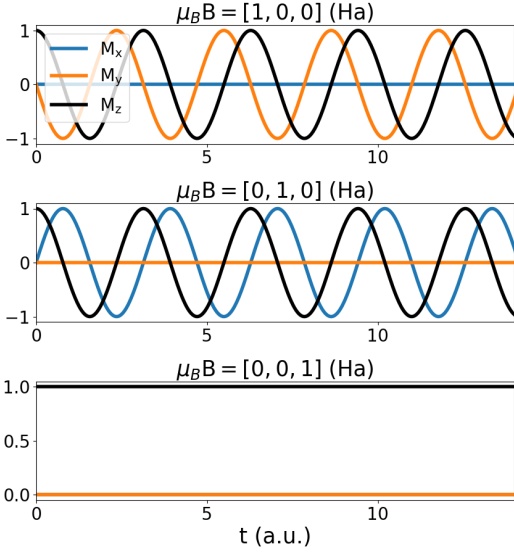
pletely uniform throughout the simulation box. We can then write

$$\dot{\mathbf{M}}_{\Omega} = 2\mu_B \mathbf{B} \times \mathbf{M}_{\Omega}(t). \quad (51)$$

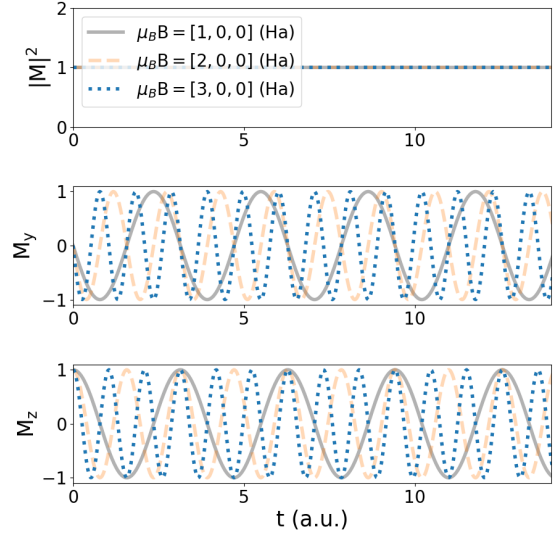
The exchange-correlation field cannot, in fact, exert a global torque on the magnetization vector. In panel (a) the external magnetic field  $\mathbf{B}$  is applied along three different directions ( $x$  in the upper plot,  $y$  in the middle and  $z$  in the lower plot). This produces perfectly oscillatory dynamics with only the component along the field axis that remains static. In the lower plot, the field is applied along the spin polarization direction  $z$ ; therefore, the atom has no dynamics. In panel (b) we do not change the magnetic field direction and instead change the amplitude and we keep the direction fixed along  $x$ . In the upper figure, the magnetization module  $|\mathbf{M}_{\Omega}|$  remains constant over time and the dynamics is fully coherent, since there is no source of dissipation. In the other two graphs we compare the  $y$  and  $z$  components of  $\mathbf{M}_{\Omega}$ . In panel (c) we compare  $\mathbf{M}_{\Omega}$  along the  $y$  axis for different values of the amplitude of the magnetic field with a sinusoidal function  $A \sin(\omega_B t)$ . The value of the oscillation frequency  $\omega_B$  is fitted to the dynamics in real time. In panel (d) the fitted value of  $\omega_B$  is shown for different values of the magnetic field amplitude. The linear relation between frequency and magnetic field is perfectly reproduced with a factor 2 consistent with Eq. (51).

### 4.6.2 bulk NiO

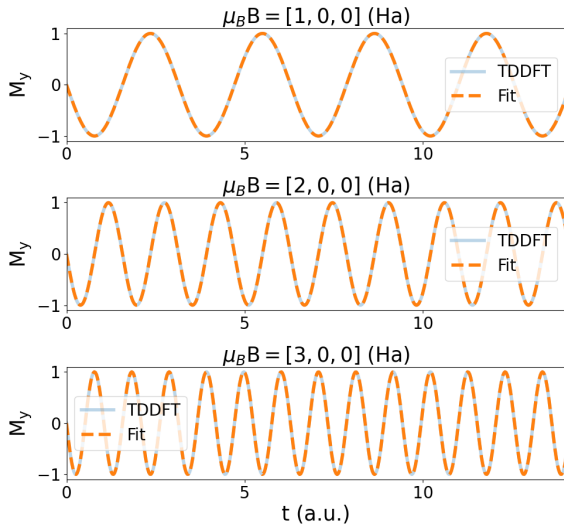
In Fig. (5) we look at the real-time dynamics of the anti-ferromagnet NiO under applied external and homogeneous magnetic fields. The electronic ground state is characterized by two opposite local magnetic moments with approximate magnitude  $1.1\mu_B$  and oriented along the  $z$ -axis localized around the two Ni atoms (the O atoms are non-magnetic). The calculation converges on a  $2 \times 2 \times 2$   $\mathbf{k}$ -grid that allows us to perform real-time simulations more efficiently. The applied magnetic field shown in the figure is oriented along the  $x$  axis and remains constant throughout the simulation. The total magneti-



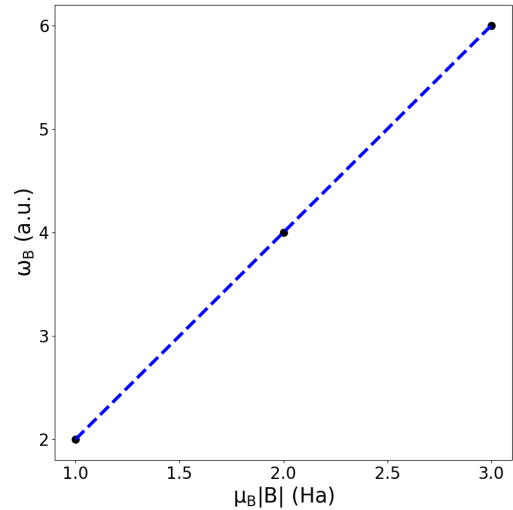
(a) H atom: magnetization under external homogeneous magnetic field oriented along three different directions.



(b) H atom: magnetization under external homogeneous magnetic field of three different amplitudes.

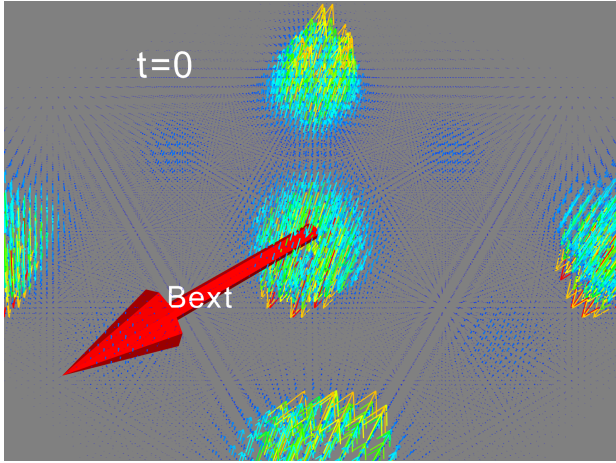


(c) H atom: fit of magnetization dynamics over sine function for different magnetic field strengths.

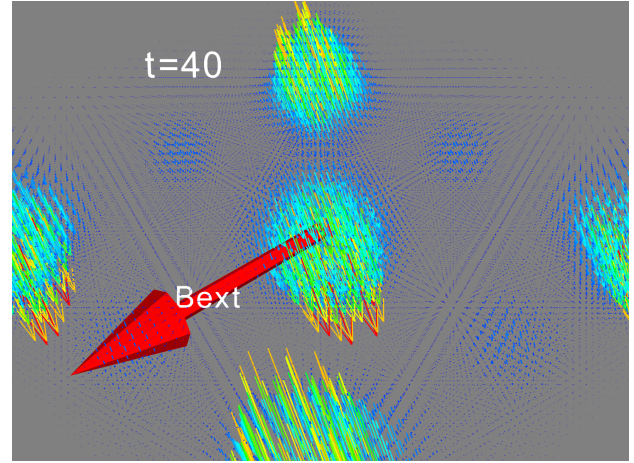


(d) H atom:  $\omega_B$  as a function of magnetic field strength.

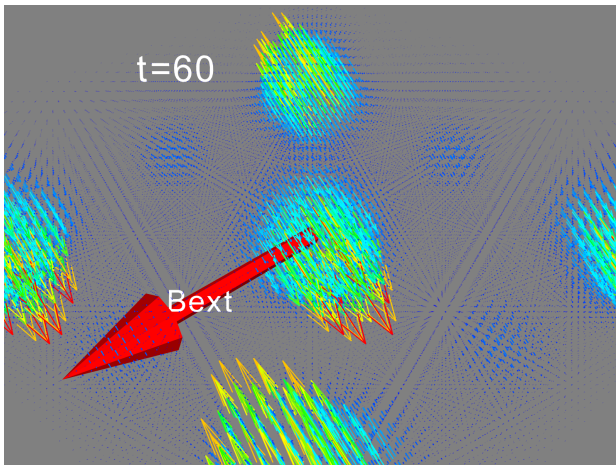
Figure 4: Time-dependent evolution of H atom under an external magnetic field. In panel (a) we compare the dynamics using fields with different polarization directions; in panel (b) we consider magnetic fields with different amplitudes; in panel (c) we fit the results against a sine function; in panel (d) we plot the oscillation frequency as a function of the field amplitude.



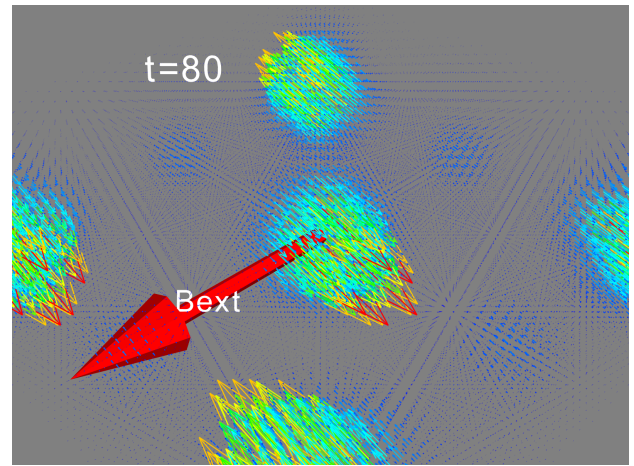
(a)  $t = 0$  steps simulation



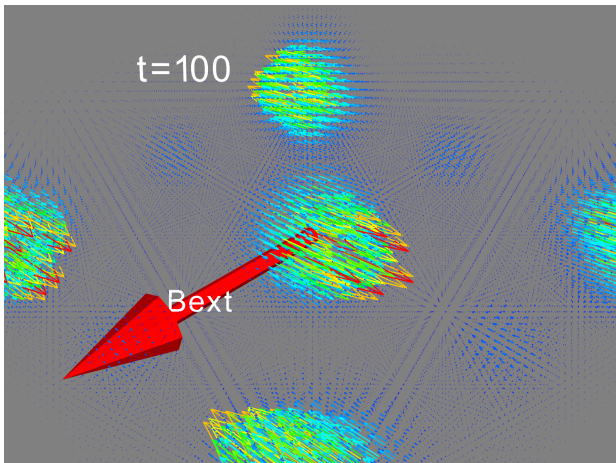
(b)  $t = 40$  steps dynamics



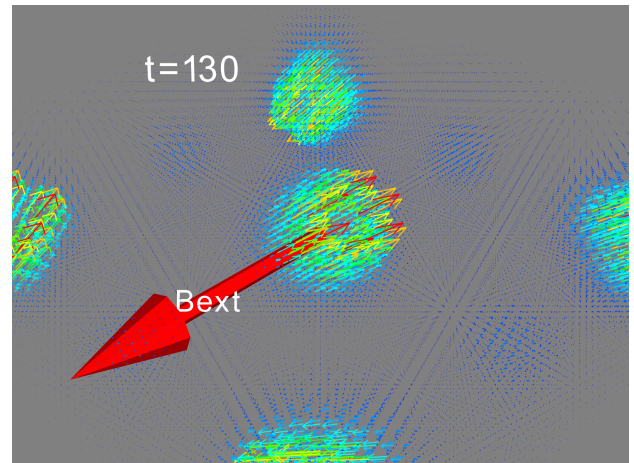
(c)  $t = 60$  steps dynamics



(d)  $t = 80$  steps dynamics



(e)  $t = 100$  steps dynamics



(f)  $t = 130$  steps dynamics

Figure 5: Time dependent evolution of NiO under an external magnetic field. The external magnetic field is applied along the x-axis and the magnetic moments are approximately aligned along the z-axis. In the different panels we show the magnetic moments precessing around the magnetic field direction over time.

zation of the system does not change over time. The system remains in its anti-ferromagnetic state. From Eq. (19) we have that the global magnetic torque acting on the anti-ferromagnet is zero. The effective equation for the two magnetic moments,  $\mathbf{M}^{A/B}$  is

$$\frac{d}{dt}\mathbf{M}^{A/B} = 2\mu_B\mathbf{B} \times \mathbf{M}^{A/B}(t) \quad (52)$$

The total magnetization  $\mathbf{M}_\Omega = \mathbf{M}^A + \mathbf{M}^B$  integrated in the cell is approximately zero in the ground state, and therefore its derivative is also zero  $\dot{\mathbf{M}}_\Omega = 0$  and its value does not change over time.

The applied magnetic field does not perturb the electronic density; as a consequence, the dynamics is adiabatic and remains fully coherent, with magnetic moments not changing in magnitude over time. In the six panels of Fig. (5) we show snapshots of the spin density profile at different time steps during the real-time simulation. The time is expressed in atomic units, and the magnetization density texture clearly shows the magnetic moments rotating around the axis parallel to the direction of the applied field. This demonstrates the capability of INQ of performing real-time spin dynamics in magnetic solids.

### 4.6.3 bcc Fe and Fe<sub>6</sub>

In Fig. (6) we look at the evolution of magnetization in the Fe<sub>6</sub> cluster and bcc Fe under an applied external magnetic field. The two systems are initially, at time  $t = 0$ , in their equilibrium ground state configuration. In both cases, the total magnetic moment is oriented along the z-axis; Fe<sub>6</sub> has a magnetic moment of approximately  $20\mu_B$ , while bcc Fe has a magnetic moment in the unit cell of  $2.22\mu_B$ . The two systems are excited using the same magnetic pulse, shown in panel (c) of Fig. (6). The dynamics is identical; the precession frequency of oscillations is the same since it is induced by the same externally applied field (with the same  $g$  factor for the two cases). We do not observe any difference in the simulation with and without spin-orbit interaction. In general, the  $g$  factor in the two cases could differ due to

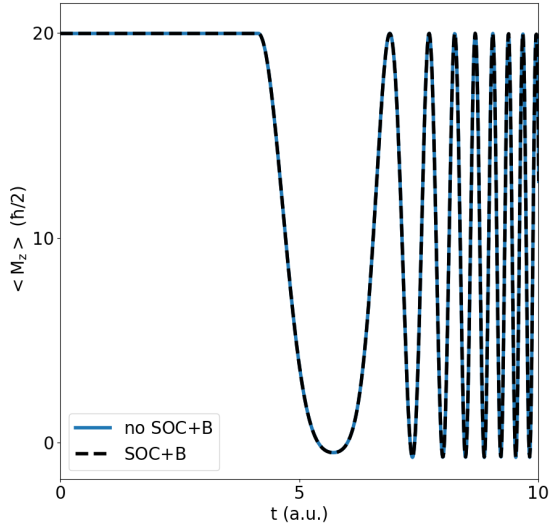
orbital angular momentum contribution,<sup>93</sup> but we are not considering this contribution here. The external magnetic field couples with the spin degrees of freedom via  $\hat{V}_z$ ; a dynamical modification of the spin-orbit requires an electronic excitation close to the nuclei that modifies the orbital state of the system. This can be obtained by applying an optical pulse; in contrast, a magnetic pulse cannot induce this type of excitation within the current implementation level. In the next section, we discuss real-time simulations in the presence of optical pulses.

## 4.7 Real-time dynamics under applied homogeneous electric fields

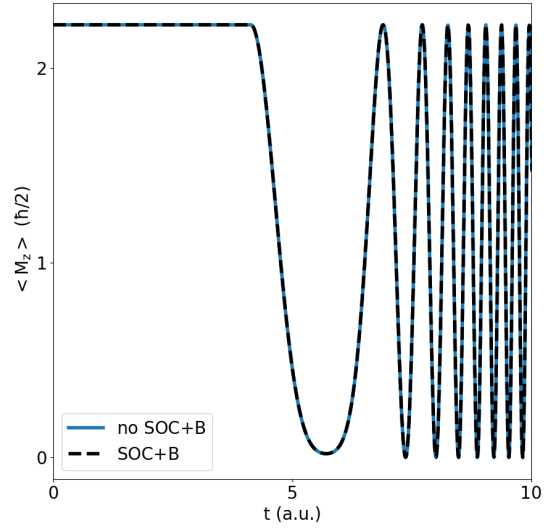
The dynamics of magnetic systems under applied external electric pulses is qualitatively different and richer compared to the dynamics under magnetic pulses alone. The applied laser pulse influences the magnetization dynamics via the spin-orbit interaction. The spin-orbit, in fact, provides a possible conversion mechanism between orbital and spin degrees of freedom. At the same time, the electric pulse excites the orbital degrees of freedom of the magnetic system and causes a charge imbalance that can induce a modification of the spin degrees of freedom. These effects have been observed experimentally<sup>18,94,95</sup> and numerically simulated using TDDFT in the case of ferromagnetic metals and magnetic clusters.<sup>85,96–100</sup> Ultrafast spin dynamics in semiconductors have been studied with first-principles density-matrix dynamics including applied pump pulses, electron-phonon, electron-electron interactions with spin-orbit couplings.<sup>93,101–103</sup>

### 4.7.1 Fe<sub>2</sub>

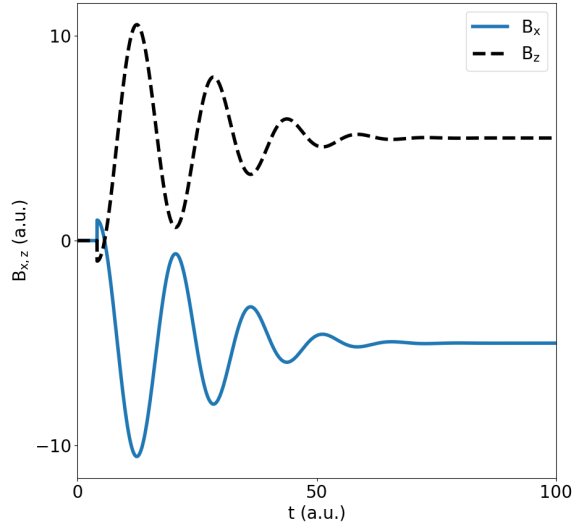
In Fig. (7) we apply a laser pulse to the Fe<sub>2</sub> cluster and study the evolution using INQ and the Octopus code.<sup>36,37</sup> The shape of the laser field is given in the figure’s caption. The initial value of the magnetization is slightly different in the two codes; we subtract this initial difference in the figure and make the two curves coincide



(a)  $\text{Fe}_6$  -  $M_z$  dynamics under an external magnetic pulse. The pulse has polarization as shown in panel (c). Dashed black line is with spin orbit and the blue line without.

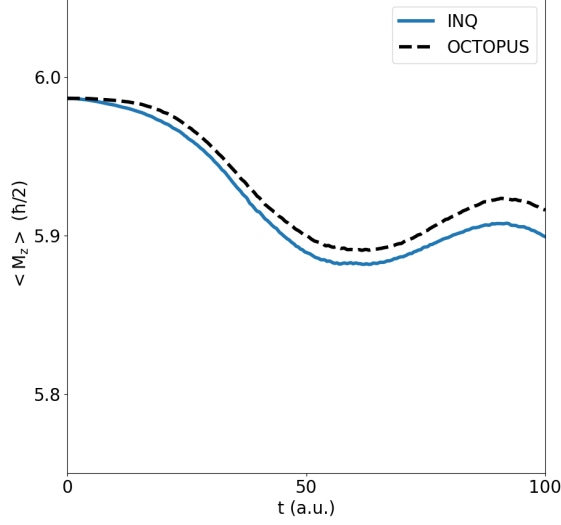


(b) bcc Fe -  $M_z$  dynamics under an external magnetic pulse. Same external pulse as in panel (a); blue line and dashed black line without and with spin-orbit interaction.

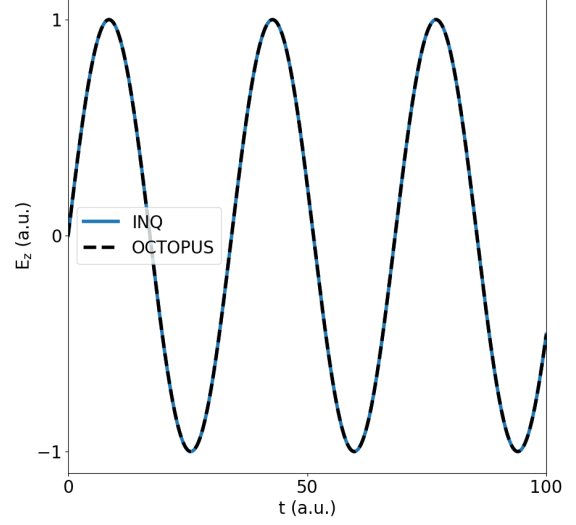


(c) Applied external magnetic pulse with polarization vector  $\boldsymbol{\epsilon} = (1\ 0\ 1)$ .

Figure 6: Time-dependent evolution of bcc Fe and  $\text{Fe}_6$  under an external magnetic pulse. The functional form of the pulse is  $\mathbf{B}(t) = A\boldsymbol{\epsilon}[\cos(\omega_0(t - t_0) + \phi) \exp(-\frac{(t-t_0)^2}{2\tau^2}) - 1]\theta(t - t_0) + \Delta\theta(t - t_0)$ . In panel (a) and (b) we look at the induced spin dynamics in  $\text{Fe}_6$  and bcc Fe. In panel (c) we show the time-dependent profile of the magnetic pulse.

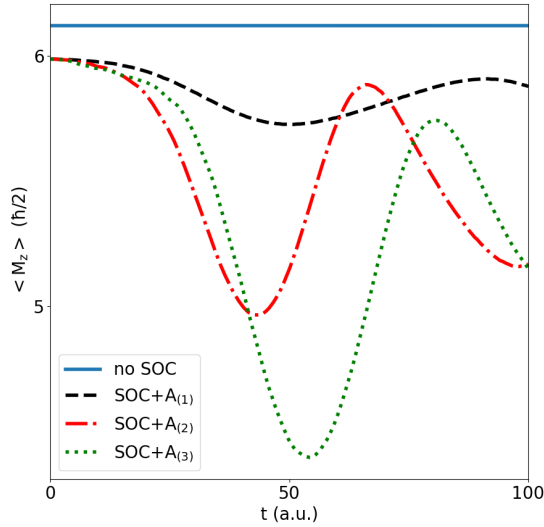


(a) Fe<sub>2</sub>:  $M_z$  dynamics under an external laser.

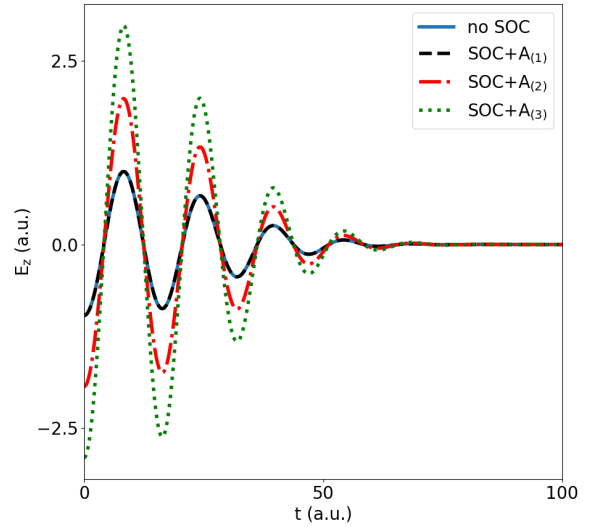


(b) Applied laser field polarized along the  $z$  direction;  $\epsilon = (0\ 0\ 1)$

Figure 7: Time dependent evolution of Fe<sub>2</sub> under an external laser field. Comparison between INQ and Octopus; the black dashed line is obtained using the Octopus code and the blue line using INQ. The laser field has shape  $\mathbf{E}(t) = A\epsilon \cos(\omega t + \phi)$ .



(a) Fe<sub>2</sub>:  $M_z$  component



(b) Fe<sub>2</sub>: applied external electric pulse with polarization  $\epsilon = (0\ 0\ 1)$  and different amplitudes  $A$ .

Figure 8: Time-dependent evolution of Fe<sub>2</sub> under three different external laser pulses. In panel (a) we look at the  $z$ -component of the magnetization of the dimer. The pulse profiles are shown in panel (b) with the same line colors and shapes. The magnetization change correlates with the pulse amplitude. The pulse temporal profile is given by  $\mathbf{E}(t) = A\epsilon \cos(\omega t + \phi) \exp\left(-\frac{(t-t_0)^2}{2\tau^2}\right)$ .

at  $t = 0$ . Qualitatively, the two curves follow a very similar behavior and the difference at longer times is due to error propagation.

In Fig. (8) we consider the same magnetic cluster  $\text{Fe}_2$  and perturb the system under different laser pulses. The temporal profile of the total magnetization is given in panel (a), the laser pulse profile is instead given in panel (b). There are four curves in the figure. The solid blue line represents the expectation value of the spin,  $\langle \hat{S}_z \rangle$ , in the absence of the spin-orbit interaction. In this case, we observe no change in the magnetization during the dynamics. This is expected given that in the absence of spin-orbit interaction there is no direct coupling between the spins and the external laser field. The black, red, and green curves are instead obtained in the presence of spin-orbit interaction, but under different amplitudes of the laser pulse as shown in panel (b) of Fig. (8). The absolute change in magnetization increases proportionally to the applied pulse amplitude. The pulses are linearly polarized along the z-axis in all the different cases. The pulse with a larger amplitude will produce transitions to higher energy orbital states with higher probability compared to the other pulses. This induces a fully coherent excitation with the system transitioning to a new electronic state with a different orbital and spin expectation value. The dynamical modification in the spin expectation value does not reflect, in general, an opposite change in the orbital expectation value given that the total electronic angular momentum is not conserved within our formalism.

Such a dynamics can be better understood starting from the pseudo-potential expression in Eq. (48). This can be rewritten in a form that makes the spin-orbit operator more explicit<sup>104</sup>

$$\begin{aligned} \hat{v}_{\text{ps}} = & \sum_{a=1}^{N_a} \left\{ V_L^a(r) + \right. \\ & \left. + \sum_{lm} |lm; a\rangle [\bar{V}_l^a(r) + V_l^{a;\text{SO}}(r) \hat{\mathbf{L}} \cdot \hat{\mathbf{S}}] \langle lm; a| \right\}. \end{aligned} \quad (53)$$

The spin operator is no longer a constant of motion in the presence of these fully relativis-

tic pseudopotentials. The time derivative of the magnetization over the volume  $\Omega$  of the simulation box can be written using Eq. (36) as

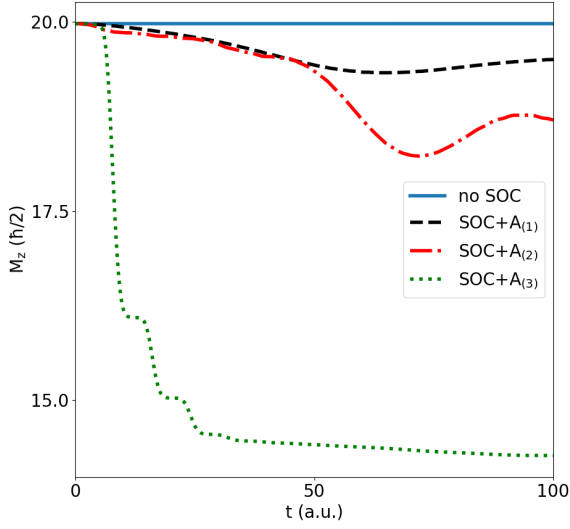
$$\begin{aligned} \frac{d}{dt} M_\Omega^i &= \int_\Omega d\mathbf{r} \Gamma_{\text{SOC}}^i(\mathbf{r}, t) = \\ &= \sum_{n\mathbf{k}} f_{n\mathbf{k}} \sum_{ju} \epsilon_{iju} \sum_{a=1}^{N_a} \sum_{mm'l} \int_\Omega d\mathbf{r} \times \\ &\times \langle n\mathbf{k} | V_l^{a;\text{SO}}(\mathbf{r} - \mathbf{R}_a) | lm; a \rangle S_{n\mathbf{k}}^u(\mathbf{r}, t) \times \\ &\times \langle lm; a | L_j | lm'; a \rangle \langle lm'; a | n\mathbf{k} \rangle, \end{aligned} \quad (54)$$

where, in the absence of an external magnetic field, we removed the other contributions in the equation. We notice that Eq. (54) is not a perfect description of the spin-orbit interaction. The internal double summation over the spherical harmonics is a potential source of problems. The summation is truncated in the calculation, neglecting the projection of the wave function on higher-order harmonics. This is ultimately a problem related to the pseudopotential approximation and to the fact that the orbital momentum operator is described on the basis of the atomic projected harmonics, which does not form a complete basis set.

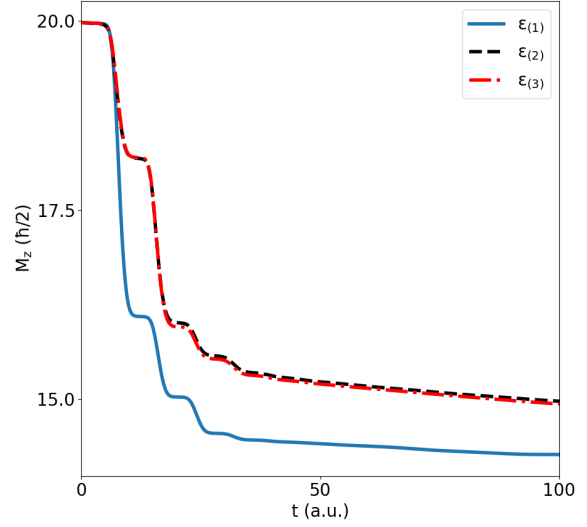
#### 4.7.2 $\text{Fe}_6$

In Fig. (9) we consider again the magnetic cluster  $\text{Fe}_6$  and perform real-time dynamics under external electric pulses. In the absence of spin-orbit interaction, we observe no magnetization dynamics consistent with the  $\text{Fe}_2$  case. This corresponds to the solid blue line in the left panel. The dashed black and red lines show a moderate demagnetization effect, which appears to be stronger for the pulse with larger amplitude. The strongest magnetization loss is observed with the pulse with the largest amplitude (the green dotted line in both panels) and amounts to approximately 27% of the initial magnetic moment of the atomic cluster. In all of the different cases, the dynamics of the magnetic moments are activated by the pulse and persist throughout its duration and even after the pulse disappears.

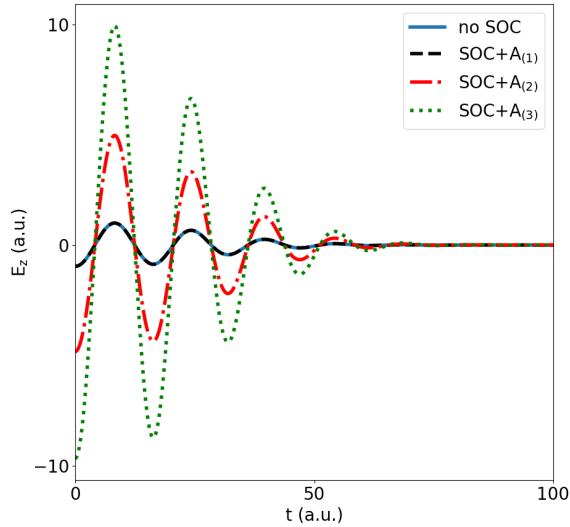
Fig. (10) shows the spin dynamics of the  $\text{Fe}_6$  cluster under electric pulses with different po-



(a)  $\text{Fe}_6$ :  $M_z$  component under laser pulses of panel (b).

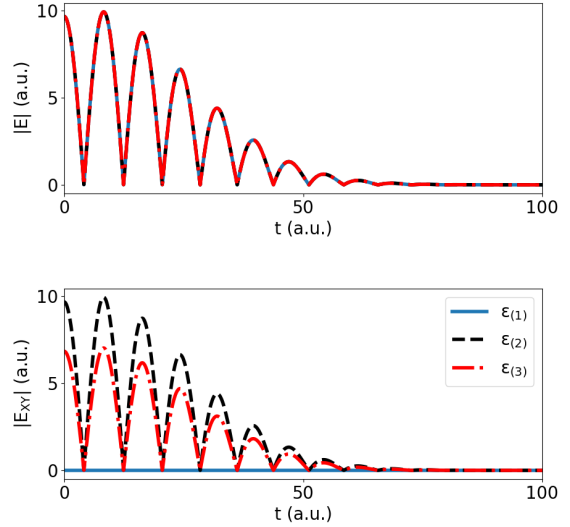


(a)  $\text{Fe}_6$ :  $M_z$  component under laser pulses of panel (b).



(b)  $\text{Fe}_6$ : applied external electric pulses. The electric field polarization is  $\epsilon = (0\ 0\ 1)$  in all three cases.

Figure 9: Time dependent evolution of  $\text{Fe}_6$  under external laser pulses. The pulse temporal profile is given by  $\mathbf{E}(t) = A\epsilon \cos(\omega t + \phi) \exp\left(-\frac{(t-t_0)^2}{2\tau^2}\right)$ . The lines in panels (a) and (b) correspond to different amplitudes  $A$ , labeled with  $A_{(1)}$ ,  $A_{(2)}$  and  $A_{(3)}$ .



(b)  $\text{Fe}_6$ : applied external electric pulses. The three lines represent different pulse polarizations with the same amplitudes.  $\epsilon_{(1)} = (0\ 0\ 1)$ ;  $\epsilon_{(2)} = (1\ 1\ 0)/\sqrt{2}$ ;  $\epsilon_{(3)} = (1\ 0\ 1)/\sqrt{2}$ .

Figure 10: Time dependent evolution of  $\text{Fe}_6$  under external laser pulses with different polarization directions. The pulse temporal profile is the same as in Fig. (9) with amplitude  $A$  unchanged.

larization directions and the same amplitudes. The magnetization profile is shown in panel (a); in panel (b, upper) we show the electric field absolute value as a function of time. The three curves overlap because the applied fields are all the same in amplitude. In panel (b, lower) we show the projection of the electric field polarization vector in the  $X - Y$  plane. Pulse (1), the blue line, has no polarization component in the plane and is fully polarized along the  $z$  axis  $(0, 0, 1)$ . Pulse (2), the dashed black line, has a polarization vector lying completely in the  $X - Y$  plane  $(1, 1, 0)/\sqrt{2}$ ; pulse (3), the red dashed line, instead has polarization  $(1, 0, 1)/\sqrt{2}$ . The results in panel (a) of Fig. (9) show a dependence of the demagnetization effect on the polarization of the electric pulse. The demagnetization is larger for the pulse polarized along the  $z$  axis. The other two pulses do not produce sensible differences in the demagnetization signal. In general, we expect such a demagnetization process to be highly dependent on the specific nature of the pulse excitation, frequency, pulse amplitude, and polarization. The polarization direction influences the orbital states excited by the pulse; in turn, this affects the change in magnetization via the spin-orbit interaction.

## 5 Conclusions

We have implemented non-collinear DFT and TDDFT in INQ. We have tested the effect of the exchange-correlation magnetic field in the locally collinear approximation, the Zeeman coupling with external magnetic fields, and the spin-orbit interaction in different systems. We compared the results with other codes available, finding good agreement. We have tested the dynamics of different magnetic systems under applied external fields, both electric and magnetic. In the presence of external magnetic fields, we recover the expected spin-precession dynamics. The dynamics under applied laser pulses are richer and predict optically driven demagnetization effects consistent with previous studies.<sup>85,98–100</sup>

This implementation sets up the stage for fu-

ture improvements like the calculation of orbital momentum dynamics, Ehrenfest dynamics for magnetic systems, and the use of functionals for better description of dynamical magnetic properties beyond the adiabatic and the locally-collinear approximation.

**Acknowledgement** We acknowledge support from the Computational Materials Sciences Program funded by the US Department of Energy, Office of Science, Basic Energy Sciences, Materials Sciences and Engineering Division for the materials application and the code development. W.F. acknowledges the support from the NSF through the University of Wisconsin Materials Research Science and Engineering Center (DMR-2309000). Part of this work was performed under the auspices of the U.S. Department of Energy by Lawrence Livermore National Laboratory under Contract No. DE-AC52-07NA27344.

## Supporting Information Available

The supporting information is available in url.

## References

- (1) Sanvito, S. In *Handbook of Materials Modeling : Methods: Theory and Modeling*; Andreoni, W., Yip, S., Eds.; Springer International Publishing: Cham, 2019; pp 1–4.
- (2) Bihlmayer, G. In *Handbook of Materials Modeling : Methods: Theory and Modeling*; Andreoni, W., Yip, S., Eds.; Springer International Publishing: Cham, 2018; pp 1–23.
- (3) Brooks, M.; Richter, M.; Sandratskii, L. In *Encyclopedia of Materials: Science and Technology*; Buschow, K. J., Cahn, R. W., Flemings, M. C., Ilshner, B., Kramer, E. J., Mahajan, S., Veyssi re, P., Eds.; Elsevier: Oxford, 2001; pp 2059–2070.

- (4) Antropov, V. P.; Katsnelson, M. I.; van Schilfgaarde, M.; Harmon, B. N. *AbInitio Spin Dynamics in Magnets. Phys. Rev. Lett.* **1995**, *75*, 729–732.
- (5) Antropov, V. P.; Katsnelson, M. I.; Harmon, B. N.; van Schilfgaarde, M.; Kusnezov, D. Spin dynamics in magnets: Equation of motion and finite temperature effects. *Phys. Rev. B* **1996**, *54*, 1019–1035.
- (6) Xu, J.; Carney, T.; Zhou, R.; Shepard, C.; Kanai, Y. Real-Time Time-Dependent Density Functional Theory for Simulating Nonequilibrium Electron Dynamics. *J. Am. Chem. Soc.* **2024**, *146*, 5011–5029.
- (7) Wu, M.; Jiang, J.; Weng, M. Spin dynamics in semiconductors. *Physics Reports* **2010**, *493*, 61–236.
- (8) Gu, Y.; Zheng, Z.; Jia, L.; Shi, S.; Zhao, T.; Zeng, T.; Zhang, Q. a. Ferroelectric Control of Spin-Orbitronics. *Advanced Functional Materials* **2024**, *34*, 2406444.
- (9) Jo, D.; Go, D.; Choi, G.-M.; Lee, H.-W. Spintronics meets orbitronics: Emergence of orbital angular momentum in solids. *npj Spintronics* **2024**, *2*, 19.
- (10) Vandersypen, L. M. K.; Eriksson, M. A. Quantum computing with semiconductor spins. *Physics Today* **2019**, *72*, 38–45.
- (11) Nagaosa, N.; Tokura, Y. Topological properties and dynamics of magnetic skyrmions. *Nature Nanotech.* **2013**, *8*, 899–911.
- (12) Göbel, B.; Mertig, I.; Tretiakov, O. A. Beyond skyrmions: Review and perspectives of alternative magnetic quasiparticles. *Physics Reports* **2021**, *895*, 1–28.
- (13) Fert, A.; Reyren, N.; Cros, V. Magnetic skyrmions: advances in physics and potential applications. *Nat. Rev. Mater.* **2017**, *2*, 17031.
- (14) Fähnle, M.; Haag, M.; Illg, C.; Mueller, B.; Weng, W.; Tsatsoulis, T.; Huang, H.; Briones, J.; Teeny, N.; Zhang, L.; Kuhn, T. Review of Ultrafast Demagnetization After Femtosecond Laser Pulses: A Complex Interaction of Light with Quantum Matter. *Am. J. Mod. Phys.* **2018**, *7*, 68–74.
- (15) Luo, J.; Lin, T.; Zhang, J.; Chen, X.; Blackert, E. R.; Xu, R.; Yakobson, B. I.; Zhu, H. Large effective magnetic fields from chiral phonons in rare-earth halides. *Science* **2023**, *382*, 698–702.
- (16) Bloom, B.; Paltiel, Y.; Naaman, R.; Waldeck, D. Chiral Induced Spin Selectivity. *Chem. Rev.* **2024**, *124*, 1950–1991.
- (17) Johansson, A. Theory of spin and orbital Edelstein effects. *Journal of Physics: Condensed Matter* **2024**, *36*, 423002.
- (18) Beaurepaire, E.; Merle, J.-C.; Daunois, A.; Bigot, J.-Y. Ultrafast Spin Dynamics in Ferromagnetic Nickel. *Phys. Rev. Lett.* **1996**, *76*, 4250–4253.
- (19) Yang, Y.; Wilson, R. B.; Gorchon, J.; Lambert, C.-H.; Salahuddin, S.; Bokor, J. Ultrafast magnetization reversal by picosecond electrical pulses. *Science Advances* **2017**, *3*, e1603117.
- (20) Kimel, A.; Kirilyuk, A.; Usachev, P.; Pisarev, R.; Balbashov, A.; Rasing, T. Ultrafast non-thermal control of magnetization by instantaneous photomagnetic pulses. *Nature* **2005**, *435*, 655–7.
- (21) Ju, G.; Hohlfeld, J.; Bergman, B.; van de Veerdonk, R. J. M.; Mryasov, O. N.; Kim, J.-Y.; Wu, X.; Weller, D.; Koopmans, B. Ultrafast Generation of Ferromagnetic Order via a Laser-Induced Phase Transformation in FeRh Thin Films. *Phys. Rev. Lett.* **2004**, *93*, 197403.
- (22) Waldeck, D. H.; Naaman, R.; Paltiel, Y. The spin selectivity effect in chiral materials. *APL Materials* **2021**, *9*, 040902.

- (23) Metzger, T. S.; Mishra, S.; Bloom, B. P.; Goren, N.; Neubauer, A.; Shmul, G.; Wei, J.; Yochelis, S.; Tassinari, F.; Fontanesi, C.; Waldeck, D. H.; Paltiel, Y.; Naaman, R. The Electron Spin as a Chiral Reagent. *Angewandte Chemie International Edition* **2020**, *59*, 1653–1658.
- (24) Banerjee-Ghosh, K.; Dor, O. B.; Tassinari, F.; Capua, E.; Yochelis, S.; Capua, A.; Yang, S.-H.; Parkin, S. S. P.; Sarkar, S.; Kronik, L.; Baczewski, L. T.; Naaman, R.; Paltiel, Y. Separation of enantiomers by their enantiospecific interaction with achiral magnetic substrates. *Science* **2018**, *360*, 1331–1334.
- (25) Yang, S.-H. Spintronics on chiral objects. *Applied Physics Letters* **2020**, *116*, 120502.
- (26) Zöllner, M.; Varela, S.; Medina, E.; Mujica, V.; Herrmann, C. Insight into the Origin of Chiral-Induced Spin Selectivity from a Symmetry Analysis of Electronic Transmission. *J. Chem. Theory Comput.* **2020**, *16*, 2914–2929.
- (27) Liu, Y.; Xiao, J.; Koo, J.; Yan, B. Chirality-driven topological electronic structure of DNA-like materials. *Nat. Mater.* **2021**, *20*, 638–644.
- (28) Fransson, J. Chiral Induced Spin Polarized Electron Current: Origin of the Chiral Induced Spin Selectivity Effect. *J. Phys. Chem. Lett.* **2025**, *16*, 4346–4353.
- (29) Chumak, A.; Vasyuchka, V.; Serga, A.; Hillebrands, B. Magnon spintronics. *Nature Physics* **2015**, *11*, 453–461.
- (30) Tancogne-Dejean, N.; Eich, F.; Rubio, A. Time-Dependent Magnons from First Principles. *Journal of Chemical Theory and Computation* **2020**, *16*, 1007–1017.
- (31) Rezende, S. *Fundamentals of Magnonics*; Springer Cham, 2020.
- (32) Yuan, H.; Cao, Y.; Kamra, A.; Duine, R. A.; Yan, P. Quantum magnonics: When magnon spintronics meets quantum information science. *Physics Reports* **2022**, *965*, 1–74.
- (33) Zhang, X. A review of common materials for hybrid quantum magnonics. *Materials Today Electronics* **2023**, *5*, 100044.
- (34) Jakowski, J.; Lu, W.; Briggs, E.; Lingerfelt, D.; Sumpter, B. G.; Ganesh, P.; Bernholc, J. Simulation of 24,000 Electron Dynamics: Real-Time Time-Dependent Density Functional Theory (TDDFT) with the Real-Space Multigrids (RMG). *Journal of Chemical Theory and Computation* **2025**, *21*, 1322–1339.
- (35) Lopata, K.; Govind, N. Modeling Fast Electron Dynamics with Real-Time Time-Dependent Density Functional Theory: Application to Small Molecules and Chromophores. *Journal of Chemical Theory and Computation* **2011**, *7*, 1344–1355.
- (36) Tancogne-Dejean, N. et al. Octopus, a computational framework for exploring light-driven phenomena and quantum dynamics in extended and finite systems. *The Journal of Chemical Physics* **2020**, *152*, 124119.
- (37) Andrade, X. et al. Real-space grids and the Octopus code as tools for the development of new simulation approaches for electronic systems. *Phys. Chem. Chem. Phys.* **2015**, *17*, 31371–31396.
- (38) Dewhurst, K.; Sangeeta, S.; Nordström, L.; Cricchio, F.; Granäs, O.; Gross, H. The Elk code. <http://elk.sourceforge.net/>.
- (39) Andrade, X.; Pemmaraju, C.; Kartsev, A.; Xiao, J.; Lindenberg, A.; Rajpurohit, S.; Tan, L.; Ogitsu, T.; Correa, A. Inq, a Modern GPU-Accelerated

- Computational Framework for (Time-Dependent) Density Functional Theory. *J. Chem. Theory Comput.* **2021**, *17*, 7447–7467.
- (40) Kohn, W.; Becke, A.; Parr, R. Density Functional Theory of Electronic Structure. *J. Phys. Chem.* **1996**, *100*, 12974–12980.
- (41) Kohn, W.; Sham, L. J. Self-Consistent Equations Including Exchange and Correlation Effects. *Phys. Rev.* **1965**, *140*, A1133–A1138.
- (42) von Barth, U.; Hedin, L. A local exchange-correlation potential for the spin polarized case. i. *Journal of Physics C: Solid State Physics* **1972**, *5*, 1629.
- (43) Jacob, C. R.; Reiher, M. Spin in density-functional theory. *International Journal of Quantum Chemistry* **2012**, *112*, 3661–3684.
- (44) Runge, E.; Gross, E. K. U. Density-Functional Theory for Time-Dependent Systems. *Phys. Rev. Lett.* **1984**, *52*, 997–1000.
- (45) van Leeuwen, R. Mapping from Densities to Potentials in Time-Dependent Density-Functional Theory. *Phys. Rev. Lett.* **1999**, *82*, 3863–3866.
- (46) Ullrich, C. A. *Time-Dependent Density-Functional Theory: Concepts and Applications*; Oxford University Press, 2011.
- (47) Capelle, K.; Vignale, G.; Györfy, B. L. Spin Currents and Spin Dynamics in Time-Dependent Density-Functional Theory. *Phys. Rev. Lett.* **2001**, *87*, 206403.
- (48) Hill, D.; Shotton, J.; Ullrich, C. A. Magnetization dynamics with time-dependent spin-density functional theory: Significance of exchange-correlation torques. *Phys. Rev. B* **2023**, *107*, 115134.
- (49) Gross, E. K. U.; Kohn, W. Local density-functional theory of frequency-dependent linear response. *Phys. Rev. Lett.* **1985**, *55*, 2850–2852.
- (50) Iwamoto, N.; Gross, E. K. U. Correlation effects on the third-frequency-moment sum rule of electron liquids. *Phys. Rev. B* **1987**, *35*, 3003–3004.
- (51) Constantin, L. A.; Pitarke, J. M. Simple dynamic exchange-correlation kernel of a uniform electron gas. *Phys. Rev. B* **2007**, *75*, 245127.
- (52) Richardson, C. F.; Ashcroft, N. W. Dynamical local-field factors and effective interactions in the three-dimensional electron liquid. *Phys. Rev. B* **1994**, *50*, 8170–8181.
- (53) Corradini, M.; Del Sole, R.; Onida, G.; Palumbo, M. Analytical expressions for the local-field factor  $G(q)$  and the exchange-correlation kernel  $K_{xc}(r)$  of the homogeneous electron gas. *Phys. Rev. B* **1998**, *57*, 14569–14571.
- (54) Dabrowski, B. Dynamical local-field factor in the response function of an electron gas. *Phys. Rev. B* **1986**, *34*, 4989–4995.
- (55) Kaplan, A. D.; Nepal, N. K.; Ruzsinszky, A.; Ballone, P.; Perdew, J. P. First-principles wave-vector- and frequency-dependent exchange-correlation kernel for jellium at all densities. *Phys. Rev. B* **2022**, *105*, 035123.
- (56) Panholzer, M.; Gatti, M.; Reining, L. Nonlocal and Nonadiabatic Effects in the Charge-Density Response of Solids: A Time-Dependent Density-Functional Approach. *Phys. Rev. Lett.* **2018**, *120*, 166402.
- (57) Dobson, J. F.; Büchner, M. J.; Gross, E. K. U. Time-Dependent Density Functional Theory beyond Linear Response: An Exchange-Correlation Potential with Memory. *Phys. Rev. Lett.* **1997**, *79*, 1905–1908.

- (58) Vignale, G.; Ullrich, C. A.; Conti, S. Time-Dependent Density Functional Theory Beyond the Adiabatic Local Density Approximation. *Phys. Rev. Lett.* **1997**, *79*, 4878–4881.
- (59) Qian, Z.; Vignale, G. Dynamical exchange-correlation potentials for an electron liquid. *Phys. Rev. B* **2002**, *65*, 235121.
- (60) Lacombe, L.; Maitra, N. Non-Adiabatic Approximations in Time-Dependent Density Functional Theory: Progress and Prospects. *Npj Computational Materials* **2023**, *9*, 124–15.
- (61) Wilken, F.; Bauer, D. Adiabatic Approximation of the Correlation Function in the Density-Functional Treatment of Ionization Processes. *Phys. Rev. Lett.* **2006**, *97*, 203001.
- (62) Perdew, J. P.; Burke, K.; Ernzerhof, M. Generalized Gradient Approximation Made Simple. *Phys. Rev. Lett.* **1996**, *77*, 3865–3868.
- (63) Tozer, D. J.; Handy, N. C. On the determination of excitation energies using density functional theory. *Phys. Chem. Chem. Phys.* **2000**, *2*, 2117–2121.
- (64) Raghunathan, S.; Nest, M. Critical Examination of Explicitly Time-Dependent Density Functional Theory for Coherent Control of Dipole Switching. *J Chem Theory Comput* **2011**, *7*, 2492–2497.
- (65) Kubler, J.; Hock, K.-H.; Sticht, J.; Williams, A. Density functional theory of non-collinear magnetism. *J. Phys. F: Met. Phys.* **1988**, *18*, 469.
- (66) Sandratskii, L. M. Noncollinear magnetism in itinerant-electron systems: Theory and applications. *Advances in Physics* **1998**, *47*, 91–160.
- (67) Pu, Z.; Li, H.; Zhang, N.; Jiang, H.; Gao, Y.; Xiao, Y.; Sun, Q.; Zhang, Y.; Shao, S. Noncollinear density functional theory. *Phys. Rev. Res.* **2023**, *5*, 013036.
- (68) Sharma, S.; Dewhurst, J. K.; Ambrosch-Draxl, C.; Kurth, S.; Helbig, N.; Pittalis, S.; Shallcross, S.; Nordström, L.; Gross, E. K. U. First-Principles Approach to Noncollinear Magnetism: Towards Spin Dynamics. *Phys. Rev. Lett.* **2007**, *98*, 196405.
- (69) Katsnelson, M. I.; Antropov, V. P. Spin angular gradient approximation in the density functional theory. *Phys. Rev. B* **2003**, *67*, 140406.
- (70) Scalmani, G.; Frisch, M. A New Approach to Noncollinear Spin Density Functional Theory beyond the Local Density Approximation. *J Chem Theory Comput.* **2012**, *8*, 2193–6.
- (71) Eich, F. G.; Gross, E. K. U. Transverse Spin-Gradient Functional for Noncollinear Spin-Density-Functional Theory. *Phys. Rev. Lett.* **2013**, *111*, 156401.
- (72) Eich, F. G.; Pittalis, S.; Vignale, G. Transverse and longitudinal gradients of the spin magnetization in spin-density-functional theory. *Phys. Rev. B* **2013**, *88*, 245102.
- (73) Pittalis, S.; Vignale, G.; Eich, F. G.  $U(1) \times SU(2)$  gauge invariance made simple for density functional approximations. *Phys. Rev. B* **2017**, *96*, 035141.
- (74) Tancogne-Dejean, N.; Rubio, A.; Ullrich, C. A. Constructing semilocal approximations for noncollinear spin density functional theory featuring exchange-correlation torques. *Phys. Rev. B* **2023**, *107*, 165111.
- (75) Dyall, K. G.; Fægri, K. J. Introduction to Relativistic Quantum Chemistry. 2007.
- (76) Liu, W.; Xiao, Y. Relativistic time-dependent density functional theories. *Chem. Soc. Rev.* **2018**, *47*, 4481–4509.
- (77) Zheng, X.; Upadhyay, S.; Wang, T.; Shayit, A.; Liu, J.; Sun, D.; Li, X. Chirality-Driven Magnetization Emerges

- from Relativistic Four-Current Dynamics. 2025; <https://arxiv.org/abs/2504.03781>.
- (78) Fröhlich, J.; Studer, U. M. Gauge invariance and current algebra in nonrelativistic many-body theory. *Rev. Mod. Phys.* **1993**, *65*, 733–802.
- (79) Lebedeva, I. V.; Strubbe, D. A.; Tokatly, I. V.; Rubio, A. Orbital magneto-optical response of periodic insulators from first principles. *Npj Comput. Mater.* **2019**, *5*.
- (80) Surh, M. P.; Li, M.-F.; Louie, S. G. Spin-orbit splitting of GaAs and InSb bands near  $\Gamma$ . *Phys. Rev. B* **1991**, *43*, 4286–4294.
- (81) Hemstreet, L. A.; Fong, C. Y.; Nelson, J. S. First-principles calculations of spin-orbit splittings in solids using non-local separable pseudopotentials. *Phys. Rev. B* **1993**, *47*, 4238–4243.
- (82) Sakurai, J. *Advanced Quantum Mechanics*; Addison-Wesley Series in Advanced Physics; Addison-Wesley, 1987.
- (83) Kleinman, L. Relativistic norm-conserving pseudopotential. *Phys. Rev. B* **1980**, *21*, 2630–2631.
- (84) Theurich, G.; Hill, N. A. Self-consistent treatment of spin-orbit coupling in solids using relativistic fully separable ab initio pseudopotentials. *Phys. Rev. B* **2001**, *64*, 073106.
- (85) Stamenova, M.; Simoni, J.; Sanvito, S. Role of spin-orbit interaction in the ultrafast demagnetization of small iron clusters. *Phys. Rev. B* **2016**, *94*, 014423.
- (86) Giannozzi, P. et al. Advanced capabilities for materials modelling with Quantum ESPRESSO. *Journal of Physics: Condensed Matter* **2017**, *29*, 465901.
- (87) Strange, P. *Relativistic Quantum Mechanics: With Applications in Condensed Matter and Atomic Physics*; Cambridge University Press, 1998.
- (88) van Setten, M.; Giantomassi, M.; Bousquet, E.; Verstraete, M.; Hamann, D.; Gonze, X.; Rignanese, G.-M. The PseudoDojo: Training and grading a 85 element optimized norm-conserving pseudopotential table. *Computer Physics Communications* **2018**, *226*, 39–54.
- (89) Kresse, G.; Furthmüller, J. Efficiency of ab-initio total energy calculations for metals and semiconductors using a plane-wave basis set. *Computational Materials Science* **1996**, *6*, 15–50.
- (90) Kresse, G.; Hafner, J. Ab initio molecular dynamics for liquid metals. *Phys. Rev. B* **1993**, *47*, 558–561.
- (91) Bousquet, E.; Spaldin, N. A.; Delaney, K. T. Unexpectedly Large Electronic Contribution to Linear Magneto-electricity. *Phys. Rev. Lett.* **2011**, *106*, 107202.
- (92) Jensen, J.; Mackintosh, A. *Rare Earth Magnetism: Structures and Excitations*; International Series of Monographs on Physics; Clarendon Press, 1991.
- (93) Xu, J.; Li, K.; Huynh, U. N.; Fadel, M.; Huang, J.; Sundararaman, R.; Vardeny, V.; Ping, Y. How spin relaxes and dephases in bulk halide perovskites. *Nat. Commun.* **2024**, *15*, 188.
- (94) Koopmans, B.; van Kampen, M.; Kohlhepp, J. T.; de Jonge, W. J. M. Ultrafast Magneto-Optics in Nickel: Magnetism or Optics? *Phys. Rev. Lett.* **2000**, *85*, 844–847.
- (95) Kirilyuk, A.; Kimel, A. V.; Rasing, T. Ultrafast optical manipulation of magnetic order. *Rev. Mod. Phys.* **2010**, *82*, 2731–2784.

- (96) Simoni, J.; Stamenova, M.; Sanvito, S. Ab initio dynamical exchange interactions in frustrated antiferromagnets. *Phys. Rev. B* **2017**, *96*, 054411.
- (97) Simoni, J.; Stamenova, M.; Sanvito, S. Ultrafast demagnetizing fields from first principles. *Phys. Rev. B* **2017**, *95*, 024412.
- (98) Krieger, K.; Elliott, P.; Müller, T.; Singh, N.; Dewhurst, J. K.; Gross, E. K. U.; Sharma, S. Ultrafast demagnetization in bulk versus thin films: an ab initio study. *Journal of Physics: Condensed Matter* **2017**, *29*, 224001.
- (99) Pellegrini, C.; Sharma, S.; Dewhurst, J. K.; Sanna, A. Ab initio study of ultrafast demagnetization of elementary ferromagnets by terahertz versus optical pulses. *Phys. Rev. B* **2022**, *105*, 134425.
- (100) Krieger, K.; Dewhurst, J. K.; Elliott, P.; Sharma, S.; Gross, E. K. U. Laser-Induced Demagnetization at Ultrashort Time Scales: Predictions of TDDFT. *J. Chem. Theory Comput.* **2015**, *11*, 4870–4874.
- (101) Xu, J.; Habib, A.; Sundararaman, R.; Ping, Y. Ab initio ultrafast spin dynamics in solids. *Phys. Rev. B Condens. Matter* **2021**, *104*, 184418.
- (102) Xu, J.; Ping, Y. Ab Initio Predictions of Spin Relaxation, Dephasing, and Diffusion in Solids. *J. Chem. Theory Comput.* **2024**, *20*, 492–512.
- (103) Li, K.; Xu, J.; Huynh, U. N.; Bodin, R.; Gupta, M.; Multunas, C.; Simoni, J.; Sundararaman, R.; Verdany, Z. V.; Ping, Y. Spin dynamics in hybrid Halide perovskites - effect of dynamical and permanent symmetry breaking. *J. Phys. Chem. Lett.* **2024**, *15*, 12156–12163.
- (104) Fernández-Seivane, F.; Oliveira, M. A.; Sanvito, S.; Ferrer, J. On-site approximation for spin-orbit coupling in linear combination of atomic orbitals density functional methods. *Journal of Physics: Condensed Matter* **2007**, *19*, 489001.